JOURNAL OF GEOPHYSICAL RESEARCH, VOL. 113, A12207, doi:10.1029/2008JA013520, 2008

Evidence and theory for trapped electrons in guide field magnetotail reconnection

J. Egedal,[1] W. Fox,[1] N. Katz,[1] M. Porkolab,[1] M. Øieroset,[2] R. P. Lin,[2,3] W. Daughton,[4] and J. F. Drake[5]

Received 20 June 2008; revised 15 August 2008; accepted 19 September 2008; published 10 December 2008.

[1] A previous analysis of electron distributions measured in situ by the Wind spacecraft has revealed that electrons were trapped in the electromagnetic geometry of the reconnection event encountered in the deep magnetotail. In this paper we develop a detailed theory that can account for the main anisotropic features of the electron distributions associated with trapping in reconnection. The analysis shows that electron trapping in electric fields is generic in reconnection, as it is required in order to maintain the condition of quasineutrality. In addition to the spacecraft data, evidence of trapping in numerical simulations is also presented. Trapping is effective in eliminating free-streaming electrons along magnetic fields and thereby reduces parallel electron currents. Its importance for fast reconnection is discussed and emphasized by observations in a laboratory plasma.

Citation: Egedal, J., W. Fox, N. Katz, M. Porkolab, M. Øieroset, R. P. Lin, W. Daughton, and J. F. Drake (2008), Evidence and theory for trapped electrons in guide field magnetotail reconnection, *J. Geophys. Res.*, *113*, A12207, doi:10.1029/2008JA013520.

1. Introduction

[2] Magnetic reconnection is a basic plasma physics phenomenon that has been investigated intensively over the past 50 years. It is the process by which magnetic field lines rearrange and change topology in the presence of a plasma [*Vasyliunas*, 1975; *Priest and Forbes*, 2000]. Although the reconnection process is localized, it has a dramatic influence on the global dynamics of the systems in which it occurs. As examples, reconnection controls the evolution of solar flares [*Giovanelli*, 1946]; it allows the solar wind to enter the Earth's magnetosphere [*Sonnerup et al.*, 1995]; and it is an integral part of magnetic substorms as observed in the magnetotail. Of special interest is the understanding of the reconnection process in the magnetotail region on the night side of the Earth, since at this location reconnection is the generator of substorms, which cause the aurora phenomena [*Nagai et al.*, 2001].

[3] Significant gains in the understanding of reconnection have been achieved through numerical and analytical work, laboratory experiments, direct in situ observations by spacecraft in the Earth's magnetosphere and by space telescopes monitoring the dynamics on the surface of the sun. There now exists growing evidence that kinetic effects related to the motion of the individual electrons are important for the structure of the reconnection region. To address such issues of fast reconnection, a much-used numerical tool is Particle-In-Cell (PIC) computer codes [*Zeiler et al.*, 2002; *Daughton et al.*, 2006]. These codes simulate the plasma from first principles, including the single particle nature of the plasma. Their numerical results have allowed for successful comparisons between the simulated magnetic reconnection geometries and those recorded in situ by spacecraft [*Phan et al.*, 2007].

[4] Another approach for gaining an understanding of reconnection and the associated kinetic effects of the electrons is to analyze the fine details of the electron data collected by spacecraft. Electrons inside a reconnection region have sampled the magnetic geometry of this region and their distribution will therefore contain information about its geometry. Thus modern spacecraft are being designed with an improved ability to measure the electron distribution function at high accuracy and resolution [*Lin et al.*, 1995].

[5] In this paper we seek to advance the understanding of the physics that controls the form of electron distributions. We thereby expand the amount of information that can be obtained directly from spacecraft observations of reconnection. In particular, our goal is to elucidate the role of trapped electrons. We find that trapping is important because it reduces parallel electron currents and therefore helps speed reconnection. Besides discussing the evidence of trapping in in-situ magnetotail observations, we also provide evidence for trapping in numerical simulations and laboratory experiments.

[6] The paper is organized as follows. In sections 2 and 3 the basic characteristics of the reconnection event encoun-

[1]Plasma Science and Fusion Center and Physics Department, Massachusetts Institute of Technology, Cambridge, Massachusetts, USA.
[2]Space Sciences Laboratory, University of California, Berkeley, California, USA.
[3]Physics Department, University of California, Berkeley, California, USA.
[4]Plasma Theory and Applications, Los Alamos National Laboratory, Los Alamos, New Mexico, USA.
[5]Institute for Research in Electronics and Applied Physics, University of Maryland, College Park, Maryland, USA.

0148-0227/08/2008JA013520$09.00

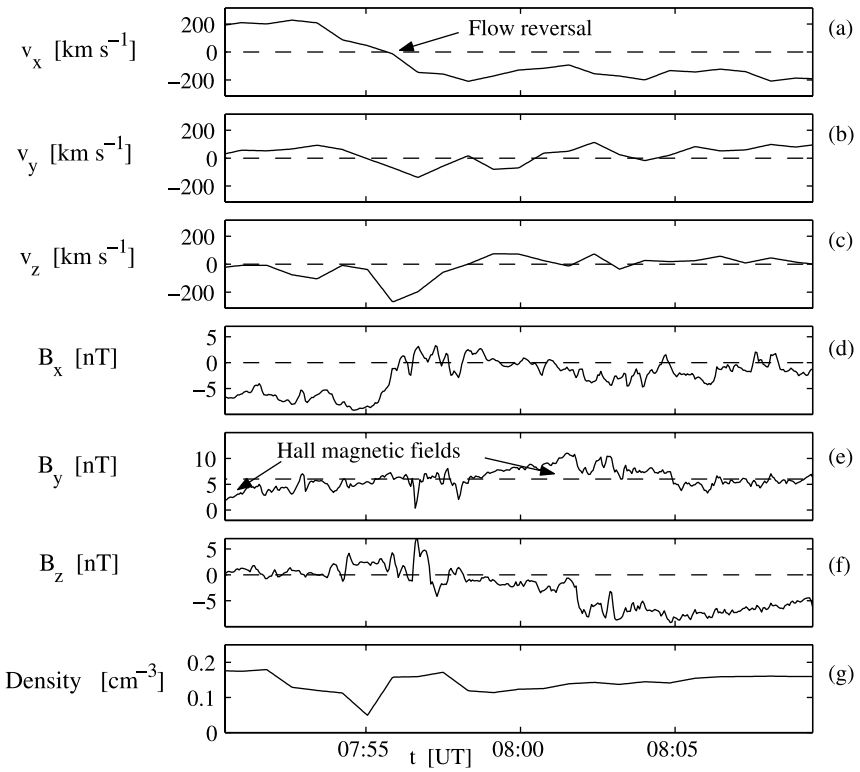

Figure 1. Wind measurements of the ion flow, the magnetic field, and the plasma density during its encounter with an active reconnection region in the distant magnetotail (60 R_E).

tered by Wind are given and our previous analysis of the event is summarized including the evidence of electron trapping. In section 4 we introduce a rigorous definition of the acceleration potential, $\Phi_{\|}$, as well as list the assumptions made for the subsequent analysis. In sections 5, 6, and 7 we analyze the effect on the electron distribution of electric trapping, magnetic trapping, and combined magnetic and electric trapping, respectively. In section 8 we provide a new analysis of the Wind data, applying the results of the previous sections. We then in section 9 show that PIC simulations include strong electric trapping and in section 10 we discuss the role of trapping in reconnection. The importance of trapping is further illustrated in section 11 where we review experimental data from the VTF laboratory experiment. Finally in section 12 the paper is concluded.

2. Reconnection Event Observed by Wind

[7] On 1 April 1999, the Wind spacecraft had a fortunate encounter with an active reconnection region deep (60 R_E) in the Earth's magnetotail. The details of the event have been described in publications by *Øieroset et al.* [2001, 2002]. The subsequent analysis by *Egedal et al.* [2005] of the observed electron distribution function showed that the electrons are trapped by electric fields in the inner reconnection region.

[8] The theory developed here on trapped electrons is motivated by the reconnection event Wind observed. Although the details of the encounter have been documented elsewhere, we find it appropriate to provide a short description of the observations most relevant to our analysis. Figure 1 displays the plasma flows, magnetic fields, and plasma density recorded during Wind's transit through the reconnection region. The reconnection event was originally identified by the reversal in the ion flow. At the time of the flow reversal the in-plane (*xz* plane) magnetic field vanished consistent with Wind travelling through an X-line geometry. The reconnection event included a moderately strong guide magnetic field ($B_y \sim 6$ nT), similar in strength to the in-plane field. The analysis of the reconnection geometry revealed the presence of the Hall magnetic fields, predicted from two-fluid models of reconnection [*Øieroset et al.*, 2001].

[9] The particle experiment on Wind [*Lin et al.*, 1995] recorded the full electron velocity distribution function f inside the reconnection region. This measurement, which covered electron energies all the way up to 300 keV, showed electron energization in the full range of energies [*Øieroset et al.*, 2002]. Here we are only concerned with the lower energy electrons, which determines the reconnection dynamics. Figure 2a illustrates the electron distribution function observed inside the reconnection region for energies up to 9 keV. The values of f are displayed for a number of different energies (listed to the right in the figure) as a function of Θ, where Θ is the pitch angle defined as the angle between the electron velocity $\mathbf{v}$ and the local magnetic field, $\cos(\Theta) = \mathbf{v} \cdot \mathbf{B}/(vB) = v_{\|}/v$. It is seen that f only has a limited dependence on Θ for energies above 6 keV, so for super-thermal energies f is isotropic. Meanwhile at lower energies f is highly anisotropic, showing reduced values for pitch angles around 90° so that $T_{\|} > T_{\perp}$.

[10] For energies in the range of 1.2 keV to 4 keV the intervals in Θ where f is reduced are limited to $\Theta \in [45°,$

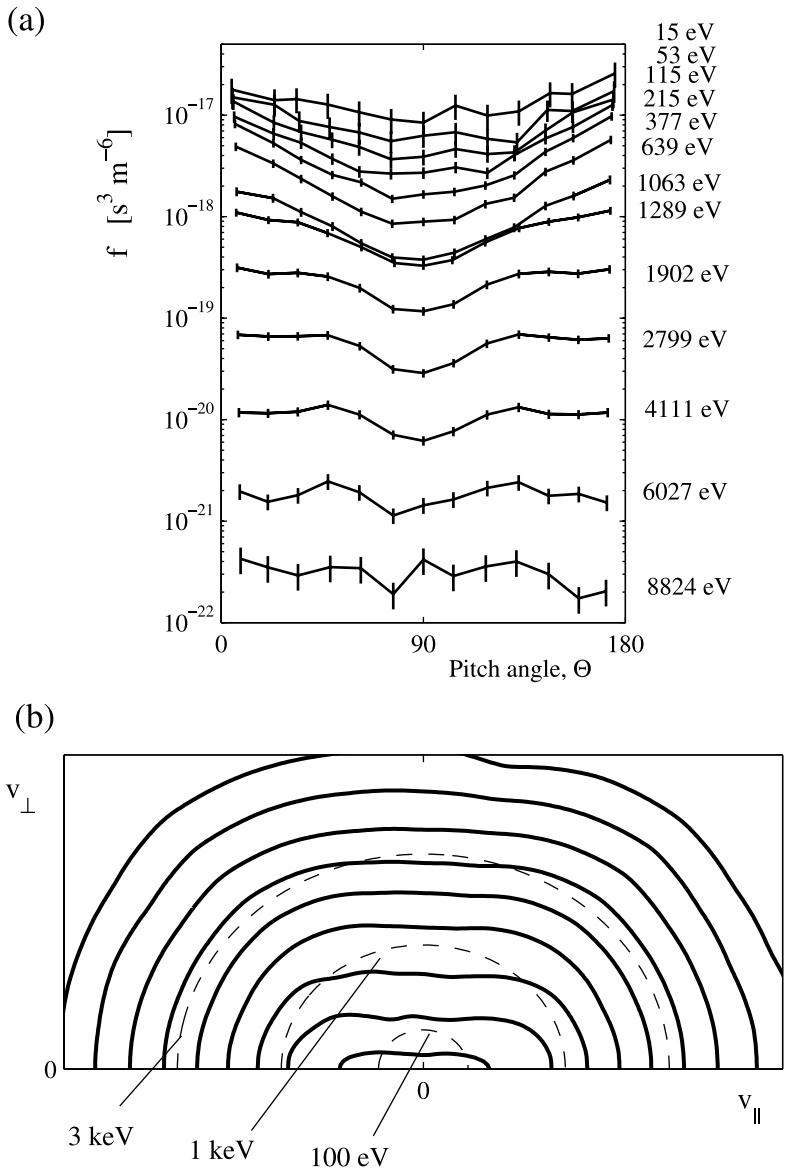

Figure 2. (a) Electron pitch angle distribution measured by the three-dimensional plasma and energetic particle instrument [*Lin et al.*, 1995] on the Wind spacecraft in the center of the reconnection region. Each line represents the phase-space density for a given energy; the respective energies are given on the right of the figure. (b) The same data as in a is displayed in terms of contours of constant f in the ($v_{\|}$, $v_{\perp}$) plane. The dashed half circles represent the electron energies, 100 eV, 1 keV, and 3 keV, respectively. The anisotropy in f causes the flattening in the contours of f observed most clearly at energies below 1 keV.

135°], whereas for energies below 1.2 keV the anisotropy extends to all pitch angles. Below we explain how these observations arise in part from the trapping of thermal electrons in electric fields.

[11] The representation applied in Figure 2a provides a detailed view of the anisotropy in f. However, this representation may be less familiar than that in Figure 2b, where the distribution is represented by contours of constant f in the ($v_{\|}$, $v_{\perp}$) plane. Here $v_{\|}$ is the velocity component along the local magnetic field and $v_{\perp}$ is the component perpendicular to the field. The dashed half circles correspond to constant electron energies (100 eV, 1 keV and 3 keV, respectively). For an isotropic distribution the contours of constant f coincide with such half circles. The anisotropy documented in Figure 2a translates into the flattening of the contours of f in Figure 2b clearly visible inside the 1 keV half circle.

[12] This anisotropy results from the interaction of the electrons with the electric and magnetic geometry as the electrons make their way into the central reconnection region. The anisotropic features in f therefore contain information about on this geometry.

3. Previous Analysis of the Measured Electron Distribution

[13] The data displayed in Figure 1 is consistent with Wind passing through the X-line geometry shown in Figure 3a.

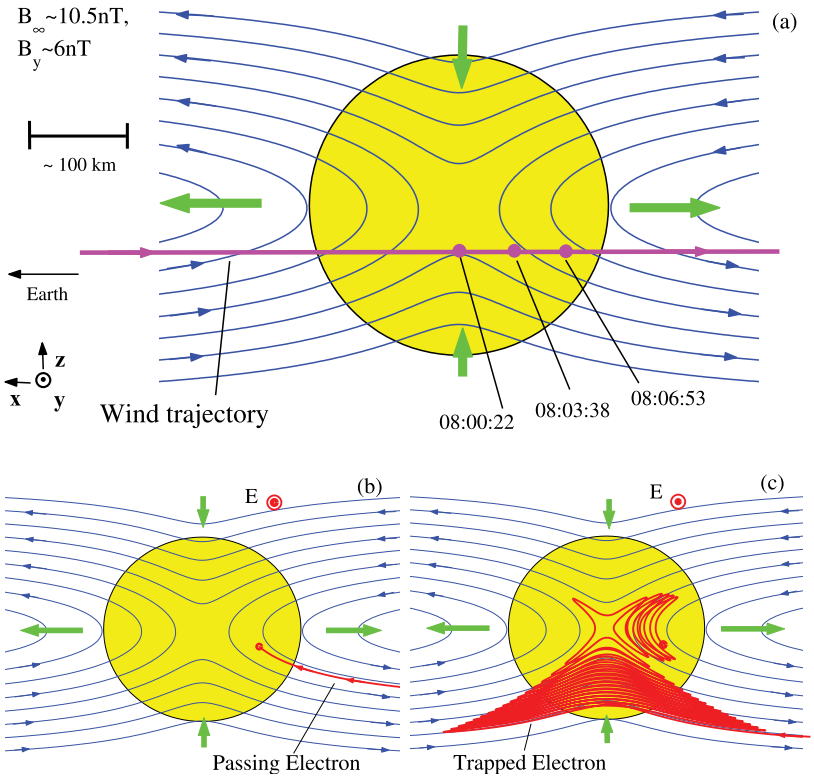

Figure 3. (a) Illustration of the magnetic geometry and the trajectory of Wind. The green arrows indicate the flow of magnetic flux toward and away from the X-line. At locations away from the X-line the in-plane magnetic field approaches values of about 11 nT. Besides the in-plane magnetic fields, an out-of-plane guide magnetic field, B_y = 6 nT, was also observed. (b) An example of a passing electron guiding center trajectory reaching the location of the Wind spacecraft. (c) An example of a trapped electron trajectory. The electron bounces back and forth along a field line, while slowly drifting with the magnetic field toward the X-line.

The in-plane magnetic field is about 8 nT just outside the reconnection region. The guide magnetic field is $B_g \sim 6$ nT and the total magnetic field strength in the ambient plasma is about $B_\infty \sim 11$ nT. The locations of Wind at three different time points are marked in Figure 3a. The electron distribution displayed in Figure 2 corresponds to the time 08:00:22 UT when Wind was closest to the X-line.

[14] In *Egedal et al.* [2005] it was shown that to understand the anisotropic features in f it is useful to consider the trajectories of the electrons entering the reconnection region. These trajectories can be divided into two categories: (1) the *passing* electrons, which enter and leave the reconnection region in a single pass along a magnetic field line and (2) the *trapped* electrons, which bounce multiple times inside the reconnection region.

[15] An example of a passing electron is shown in Figure 3b; it follows a field line in a straight shot into the reconnection region, where it is intercepted by the spacecraft. In the absence of a spacecraft it will continue to follow the field-line out of the region. Figure 3c provides an example of a trapped electron, which bounces back and forth along one particular field line. It approaches the inner reconnection region as this field line convects slowly (compared to v_{th}) into the X-line region and reconnects. The field line is then ejected from the region at the Alfvén speed, which is also small compared to v_{th} of the electrons. Thus the trapped electrons will continue their bounce motion in the outflow region.

[16] The anisotropic features were analyzed by applying Liouville's theorem, which states that $df/dt = 0$ along the electron trajectories. It follows that the phase space density $f(\mathbf{x}_0, \mathbf{v}_0)$ for a point $(\mathbf{x}_0, \mathbf{v}_0)$ inside the diffusion region is identical to $f_\infty(\mathbf{x}_\infty, \mathbf{v}_\infty)$ where $(\mathbf{x}_\infty, \mathbf{v}_\infty)$ is a point on the electron trajectory in the ambient plasma. The electron distribution in the ambient plasma f_∞ is assumed isotropic, so to determine

$$f(\mathbf{x}_0, \mathbf{v}_0) = f_\infty(\mathbf{x}_\infty, \mathbf{v}_\infty) = f_\infty(\mathcal{E}_\infty), \tag{1}$$

we need only characterize the kinetic energy $\mathcal{E}_\infty$ that the electron had before it entered the reconnection region. The energy $\mathcal{E}_\infty$ was obtained by numerical integration of electron trajectories in a simple X-line geometry. Trajectories were followed back in time from a phase space point $(\mathbf{x}_0, \mathbf{v}_0)$ until the trajectories reached the ambient plasma and $\mathcal{E}_\infty$ was evaluated.

[17] To reproduce the anisotropic features in f at energies below 1 keV it was necessary to introduce an electric potential. In this paper we will denote this potential as the acceleration potential, $\Phi_\parallel$. The change of $\Phi_\parallel$ between the reconnection region and the ambient plasma was found to be 1 kV ($\sim 2.5\ T_e/e$); hence all thermal electrons were

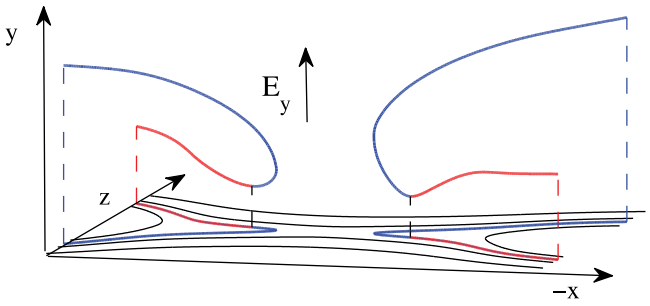

Figure 4. Based on kinetic simulation data, two three-dimensional magnetic field lines are shown above their in-plane projections. Because of the Hall magnetic field perturbation, B_y changes sign (blue sections, $B_y < 0$; red sections, $B_y > 0$). The nearly uniform E_y can help trap electrons in the vicinity of the field lines' local minima in y.

trapped. In the next section it is clarified that the acceleration potential is not the regular in-plane potential, Φ. Rather, $\Phi_{\|}$ is a measure of the work by electric fields on an electron as it escapes the region along a magnetic field line. We find that $\Phi_{\|}$ and Φ in general are significantly different because $\Phi_{\|}$ includes important contributions from inductive electric fields.

[18] While the analysis by *Egedal et al.* [2005] showed that the thermal electrons are trapped in electric fields, it did not provide an explanation for why this trapping develops. In this paper, rather than solving for f numerically, we apply a constants of motion approach, which yields an analytical understanding of the kinetic effects that govern the electron dynamics. The analysis shows that trapping is essential for maintaining quasineutrality inside the reconnection region, and it can therefore be expected to be generic in reconnection.

4. Acceleration Potential $\Phi_{\|}$ and Model Assumptions

[19] Because of the three-dimensional geometry of the magnetic field lines in the reconnection region, it is not just the in-plane potential, Φ, that determines if an electron is trapped by electric fields. Both in-plane and out-of-plane inductive electric fields generally have components along the magnetic field lines which are important for trapping. To accurately describe trapping while including all electrical field components, we introduce the acceleration potential $\Phi_{\|}$ as a measure of the work done by electric fields on a passing electron as it escapes the reconnection region in a straight shot along a magnetic field line. Therefore mathematically $\Phi_{\|}$ must be defined as

$$\Phi_{\|}(\mathbf{x}) = \int_{\mathbf{x}}^{\infty} \mathbf{E} \cdot d\mathbf{l}, \tag{2}$$

where the integration is carried out along the magnetic field from the point $\mathbf{x}$ to the point where the field line reaches the uniform ambient plasma. From this definition, it is clear that $\Phi_{\|}$ is only a pseudo-potential because the gradient of $\Phi_{\|}$ perpendicular to the magnetic field has no physical importance. Furthermore, in contrast to the regular potential Φ, the acceleration potential also depends on the overall magnetic structure and all the three components of $\mathbf{E}$, including the inductive electric fields.

[20] In particular for near-antiparallel reconnection (small guide magnetic field) the reconnection electric field, E_y, together with the familiar Hall magnetic field perturbation can provide a significant contribution to $\Phi_{\|}$. As an example, in Figure 4 we consider the three-dimensional geometry of representative field lines of the kinetic simulation presented in section 9. The force of E_y on electrons can cause trapping in the vicinity of the field lines' local minima in y. The minima are due to the Hall magnetic field perturbation, causing B_y to reverse sign.

[21] Given the contributions from inductive electric fields, the integral in equation (2) is path dependent and it is unlikely that $\Phi_{\|}$ can be observed directly by spacecraft, because a spacecraft in general does not follow a particular field line as it enters a reconnection region (required for carrying out the integral in equation (2)). Furthermore, the parallel electric field in a plasma is small, which often prohibits its measurement; the values of $\Phi_{\|}$ only become significant because the integration length in equation (2) spans several ion inertial lengths. However, $\Phi_{\|}$ can be evaluated directly in numerical simulations. In fact, in section 9 we give an example of a numerical simulation that confirms the existence of the acceleration potential consistent with that inferred above in the Wind observations.

[22] In the following sections we develop a theory which provides an analytical approximation for f that accounts for the main anisotropy prevalent in the Wind observations. The theory represents the zeroth order term f_0 in an expansion of $f = f_0 + (\langle v \rangle / v_{th}) f_1 + \ldots$, where $\langle v \rangle = |\int \mathbf{v} f d^3v|/n$ is the magnitude of the mean electron drift speed and v_{th} is the electron thermal speed. Thus the theory is accurate for calculating even moments of f, such as $n = \int f d^3v$ and $\mathbf{p} = \int (\mathbf{v} - \langle \mathbf{v} \rangle)(\mathbf{v} - \langle \mathbf{v} \rangle) f d^3v$. Furthermore, for known magnetic and electric fields and a given f_0, the mean perpendicular drift, $\langle \mathbf{v}_{\perp} \rangle$, is readily obtained from the perpendicular momentum balance of the electrons and the mean parallel drift, $\langle v_{\|} \rangle$, can then be obtained from the continuity equation $\nabla_{\|}(n\langle v_{\|} \rangle) + \nabla_{\perp} \cdot (n\langle \mathbf{v}_{\perp} \rangle) + \partial n/\partial t = 0$.

[23] We will build up the theory in steps considering increasingly complicated electromagnetic geometries, but before doing so we find it useful to state all the assumptions, which the final theory relies on:

[24] 1. The electron dynamics are described by Liouville's theorem: $df/dt = 0$.

[25] 2. The magnetic moment of the electrons, μ, is conserved.

[26] 3. The electron mass is small and the electron temperature is large such that their thermal speed is much larger than any other velocity in the system.

[27] 4. The reconnection/X-line region is imbedded in a current sheet. Following the magnetic field lines of the reconnection region sufficiently far away they reach a uniform current sheet with $\mathbf{E} \cdot \mathbf{B} = 0$.

[28] 5. In the parts of the ambient plasma that feed the electrons to the reconnection region the magnetic field strength is uniform.

[29] 6. In the parts of the ambient plasma that feed the electrons to the reconnection region the distribution of the incoming electrons, f_{∞}, is isotropic and uniform.

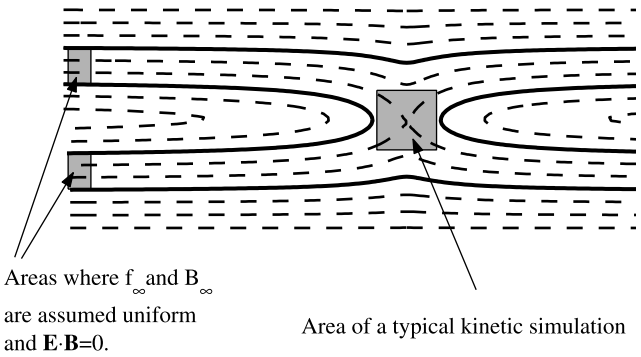

Figure 5. Illustration of the general geometry considered. The assumptions 4 to 6 apply only to the regions shaded far away from the reconnection X-line. Therefore these assumptions do not require the inner reconnection region to be symmetric.

[30] As illustrated in Figure 5 the assumptions (4) to (6) apply only to regions in the ambient plasma far away from the X-line. The inner reconnection region considered in kinetic simulations is also outlined in Figure 5; this inner region is not assumed to be symmetric. Furthermore, while we consider here only two-dimensional magnetic geometries the model can be generalized also to three dimensions. However, three-dimensional effects such as turbulence and dynamics involving electron holes [*Drake et al.*, 2003; *Daughton et al.*, 2004] often break the adiabatic invariance of μ and are therefore not included in the theory.

[31] For simplicity our ''cartoon'' illustrations of the magnetic geometries and electric field structures are often symmetric about the X-line, but we stress again that the developed model does not rely on such symmetries of the inner region. In fact, our model is fully compatible with the numerical simulation presented in section 9 that includes nonsymmetric structures related to the presence of a guide magnetic field.

5. Trapping in Electric Fields

[32] In this section we discuss how electric trapping influences the distribution function of the electrons. The derivations rely on the electron thermal speed, v_{th}, being much larger than the speed at which field lines convect into the reconnection region. Because of the small electron mass this is in general a good approximation. The expressions derived for f are exact in the limit where $m_e \rightarrow 0$ for fixed T_e.

[33] We start out by analyzing electric trapping in the simple and idealized geometry shown in Figure 6 consisting of a uniform magnetic field $\mathbf{B} = -B\hat{\mathbf{x}}$ in the negative x direction, which is moving with constant velocity, $\mathbf{v} = -v_z\hat{\mathbf{z}}$, in the negative z direction. This motion reflects an inductive electric field $\mathbf{E}_y = -v_z B\hat{\mathbf{y}}$ in the negative y direction. Furthermore, an in-plane potential $\Phi(x, z)$ is outlined by the diamond shaped contours. Inside the region where the potential is finite the electric field is given by $\mathbf{E} = a(x/|x|)\hat{\mathbf{x}} + b(z/|z|)\hat{\mathbf{z}}$, where a and b are positive constants and $\hat{\mathbf{x}}$ and $\hat{\mathbf{z}}$ are the unit-vectors. Note that we have chosen the coordinate system and the directions of the fields to be similar to those seen in the upper inflow region of Figure 3a. Furthermore, note also that in this idealized geometry where (1) the inductive electric field is perpendicular to the magnetic field and (2) the ambient potential is uniform, we have $\Phi_{\|} = \Phi$.

[34] The present field configuration allows for a simple analysis of the electron kinetics. The guiding center trajectory in Figure 6 represents an electron trapped by the electric fields. Outside the trapping region it travels with the magnetic field in the $-z$ direction while moving with a small parallel velocity along the field. As it reaches the diamond shaped region of finite potential, $\Phi_{\|}$, the electron is first accelerated by the parallel electric fields, E_x. The sign of E_x is reversed at $x = 0$ causing $v_{\|}$ to decrease for $x < 0$ (to the right in the figure). The electron becomes trapped because the drift in the $-z$ direction has pushed the electron deeper into the trapping region.

[35] Once the electron is trapped, its parallel motion is controlled by the second adiabatic invariant $J = \oint v_{\|} dl = \oint v_x dx$, which is the integral of $v_{\|}$ over a bounce period. Given that E_x is independent of y and symmetric about $x = 0$, in order for J to be conserved the trapped section of the trajectory has the periodic shape shown in Figure 6, where $|v_x|$ is a function of x only (independent of y and z).

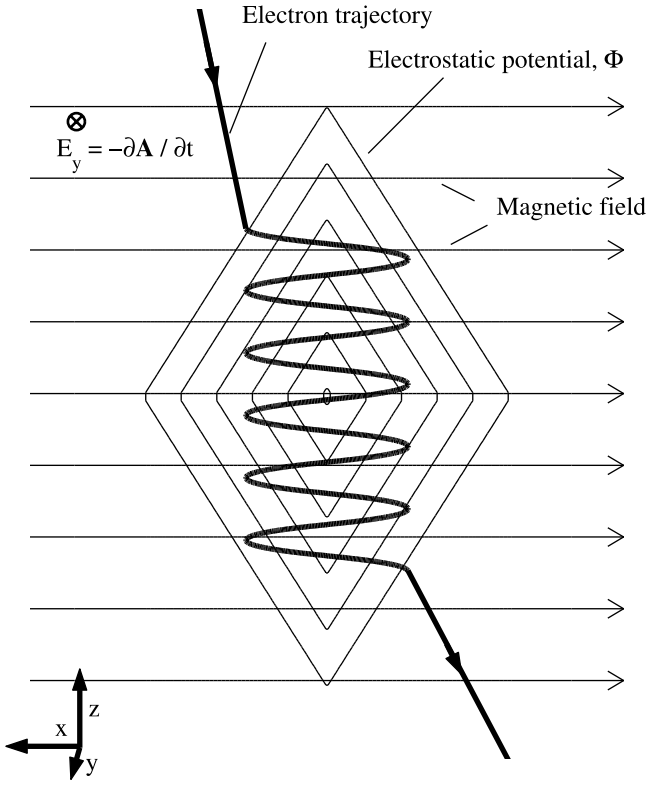

Figure 6. Illustration of an electron trapped by electric fields. The geometry includes a uniform magnetic field B_x, moving downward at the speed $v_z = E_y/B_x$. The diamond-shaped contours outline the form of a acceleration potential $\Phi_{\|}$. The trajectory shows electron temporarily trapped in the potential structure.

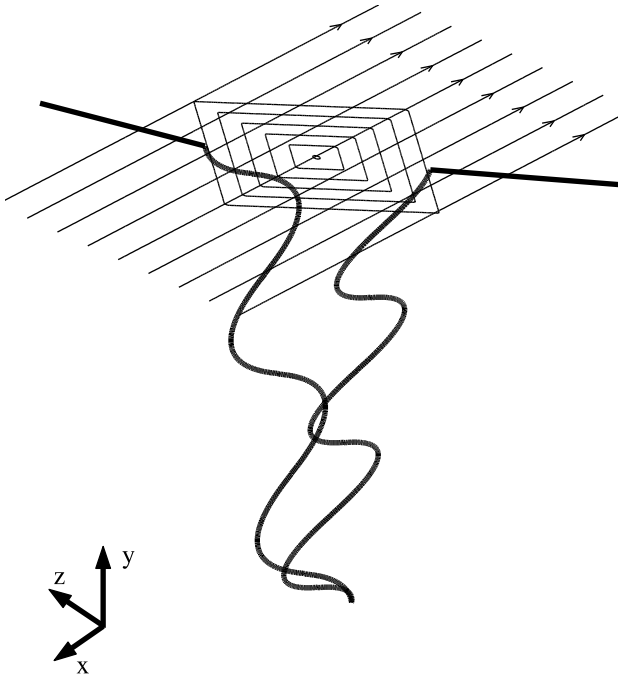

Figure 7. Perspective view of the same configuration as in the previous figure. Inside the trapping region the electron travels a significant distance in the $-y$ direction. This motion is important of the overall energy balance of the trapped electrons.

[36] The motion in the y direction can be understood based on the requirement of energy conservation. In the uniform magnetic field the magnetic moment $\mu = mv_\perp^2/(2B)$ is conserved and it is clear that $v_\perp$ is constant along the trajectory. Therefore the energy balance only includes the parallel kinetic energy $\mathcal{E}_\parallel = mv_\parallel^2/2$ and can be expressed as

$$\mathcal{E}_{\parallel\infty} = \mathcal{E}_\parallel(x) + e\big(\Delta y\, E_y - \Phi_\parallel(x,z)\big). \tag{3}$$

Here $\mathcal{E}_{\parallel\infty}$ is the initial value of $\mathcal{E}_\parallel$ outside the trapping region and Δy is the distance traveled in the y direction. Again, inside the trapping region $\mathcal{E}_\parallel$ is a function of x only, $\mathcal{E}_\parallel = \mathcal{E}_\parallel(x)$ and, therefore the z dependence of $\Phi_\parallel(x,z)$ in equation (3) can only be balanced by the $\Delta y E_y$ term. This requires $\Delta y = \Delta y(z)$ consistent with the trajectory in Figure 7 showing how the electron travels in the $-y$ direction as the center of the trapping region is approached. The motion in the y direction can also be understood as the electrons E $\times$ B drifting in the perpendicular electric fields without getting energized [*Wygant et al.*, 2005]. As illustrated here this drift allows electrons to become deeply trapped in $\Phi_\parallel$.

[37] Understanding the kinetic behavior of the trapped electrons allows us to analyze the anisotropic features that can be expected in $f(\mathbf{x}_0, \mathbf{v}_0)$ at a location, $\mathbf{x}_0$, inside the trapping region. Above in section 3 we obtained equation (1) ($f(\mathbf{x}_0, \mathbf{v}_0) = f_\infty(\mathcal{E}_\infty)$) from Liouville's theorem, where f_∞ is assumed to be a uniform isotropic distribution characterizing the ambient plasma.

[38] As illustrated in Figure 8, the key to solving equation (1) analytically is to consider separately the trapped and passing electrons when determining their values of $\mathcal{E}_\infty$. In the limit where the parallel velocity in the bounce motion is much larger than the drift speed in the $-z$ direction only electrons with small initial values of $\mathcal{E}_{\parallel\infty}$ will become trapped in the acceleration potential. Consider the trapped trajectory in Figure 8. This electron is marginally trapped because its first turning point is at the boundary of the acceleration potential. From energy conservation it is clear the initial parallel energy is $\mathcal{E}_{\parallel\infty} = e(\Delta x_2 - \Delta x_1)E_x$, where Δx_1 and Δx_2 are defined in the

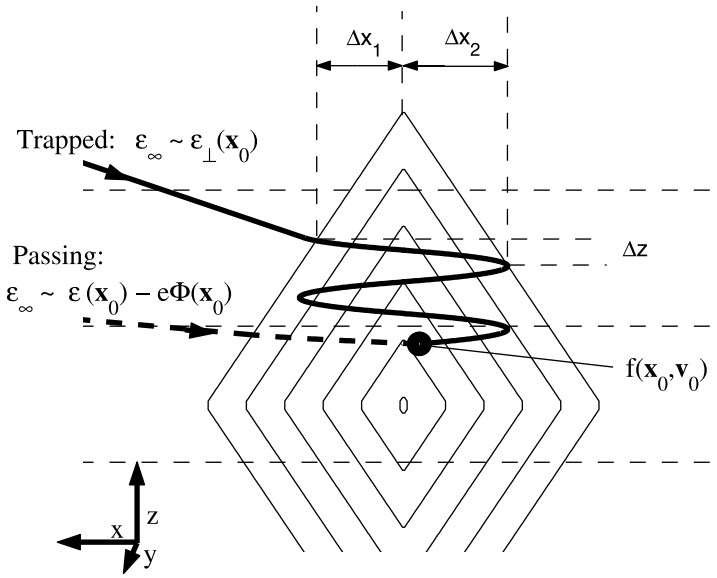

Figure 8. To characterize $f(\mathbf{x}_0, \mathbf{v}_0)$ using Liouville's theorem, trajectories are categorized as passing or trapped. The energy in the ambient plasma for the two categories $\mathcal{E}_\infty$, have distinct mathematical representations.

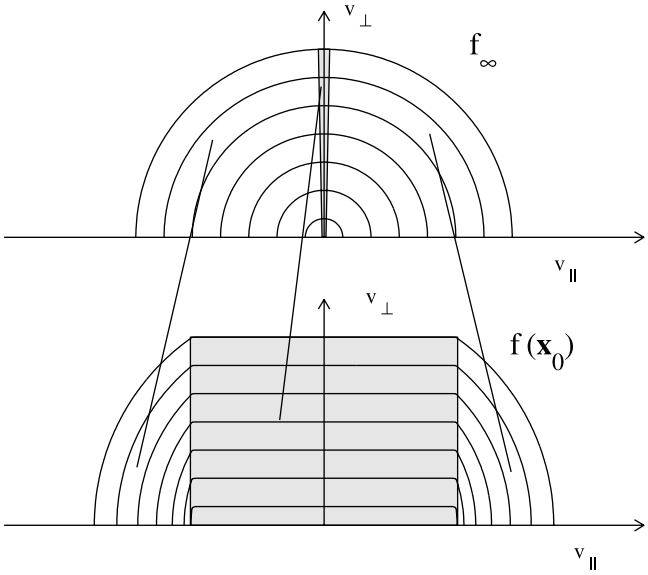

Figure 9. Illustration of the distribution function in the ambient plasma f_∞ and in the trapping region $f(\mathbf{x}_0)$. The acceleration potential makes $f(\mathbf{x}_0)$ nonisotropic. In $f(\mathbf{x}_0)$ all passing electrons have gained a parallel energy of $e\Phi_\parallel$. The shaded region in $f(\mathbf{x}_0)$ corresponds to trapped electrons with $v_\parallel < \sqrt{2e\Phi_\parallel/m}$. In the ambient distributions the trapped electrons all originate from a small region with $|v_\parallel| \ll v_\perp$.

figure. Now because $\Phi_\parallel$ for the present configuration coincides with the regular potential we have that $(\Delta x_2 - \Delta x_1)E_x = \Delta z E_z$. The distance travelled in the z direction can be expressed as $\Delta z = v_z t_b$, where the bounce time can be approximated as $t_b = 2(x_1 + x_2)/v_{th}$. Hence we find that $\mathcal{E}_{\parallel\infty} \simeq 2(x_1 + x_2)E_z v_z/v_{th}$. For a typical reconnection geometry we estimate that $E_z \simeq 10\ E_x$ and $v_z \simeq v_A/10 \simeq v_{th}/400$. Using that $2(x_1 + x_2)E_x \simeq 4\ T_e$ we find that $\mathcal{E}_{\parallel\infty} \simeq T_e/10$ represents the maximal value that is compatible with electrons becoming trapped. Meanwhile, for the typical electron we have $\mathcal{E}_{\perp\infty} \sim T_e$ and it follows that trapped electrons are characterized by $\mathcal{E}_{\parallel\infty} \ll \mathcal{E}_{\perp\infty}$. Therefore the total kinetic energy in the ambient plasma is approximated by

$$\mathcal{E}_\infty \simeq \mathcal{E}_\perp(\mathbf{x}_0) \qquad \text{when trapped.} \tag{4}$$

[39] For the passing electrons $\mathcal{E}_{\parallel\infty}$ can be obtained from equation (3). When the drift speed of the magnetic field lines is small compared to the electron thermal speed, $v_z \ll v_{th}$, the $\Delta y E_y$ term can be neglected for a single pass through the region. Thus for the passing electrons it follows that $\mathcal{E}_{\parallel\infty} = \mathcal{E}_\parallel(\mathbf{x}_0) - e\Phi_\parallel(\mathbf{x}_0)$. Adding the constant perpendicular energy component to this we find

$$\mathcal{E}_\infty \simeq \mathcal{E}(\mathbf{x}_0) - e\Phi_\parallel(\mathbf{x}_0) \qquad \text{when passing.} \tag{5}$$

[40] Using equations (1), (4), and (5) we may now express the distribution, $f(\mathbf{x}_0, \mathbf{v}_0)$, in the trapping region as

$$f(\mathbf{x}_0, \mathbf{v}_0) = \begin{cases} f_\infty(\mathcal{E}_\perp(\mathbf{x}_0)) & , \quad \text{trapped} \\ f_\infty\big(\mathcal{E}(\mathbf{x}_0) - e\Phi_\parallel(\mathbf{x}_0)\big), & \text{passing} \end{cases}, \tag{6}$$

where the trapped/passing boundary is found by solving $\mathcal{E}_{\parallel\infty} = \mathcal{E}_\parallel(\mathbf{x}_0) - e\Phi_\parallel(\mathbf{x}_0) = 0$, because a particle that barely escapes will have depleted its parallel energy by the time it reaches the ambient plasma.

[41] A remarkable feature of equation (6) is that it only depends on the local value of $\Phi_\parallel(\mathbf{x}_0)$ and is independent of the detailed geometry of $\Phi_\parallel$. Thus in the limit where $v_{th} \gg v_z$, equation (6) is general and holds independent of the form and structure of $\Phi_\parallel$.

[42] Contours of constant f_∞ and $f(\mathbf{x}_0)$ in the $(v_\parallel, v_\perp)$ plane are given in Figure 9. The figure summarizes our findings above of how the isotropic distribution in the ambient plasma is modified in the trapping region as described by equation (6). When entering from the ambient plasma all passing electrons experience a gain of $e\Phi_\parallel(\mathbf{x}_0)$ in parallel kinetic energy while their perpendicular kinetic energy is unchanged. The trapped electrons fill the region $|v_\parallel| \le \sqrt{2e\Phi_\parallel(\mathbf{x}_0)/m_e}$; they all originate with $v_\parallel \sim 0$ in the ambient plasma. Thus their gains in $\mathcal{E}_\parallel$ are in the range of 0 to $e\Phi_\parallel(\mathbf{x}_0)$ and, like the passing electrons, their perpendicular energy is conserved. As shown in the figure, these transformations map the contours of f_∞ onto the contours of $f(\mathbf{x}_0)$.

[43] Figure 10 also illustrates f_∞ and $f(\mathbf{x}_0)$, but now in the representation where f is given as a function of Θ for a number of different energies. The isotropic f_∞ is independent of Θ (see Figure 10a). In Figure 10b it is observed that $f(\mathbf{x}_0)$ is identical to f_∞ for $\Theta = 90°$. At all other values of Θ we have $f(\mathbf{x}_0) > f_\infty$ corresponding to the electrons being

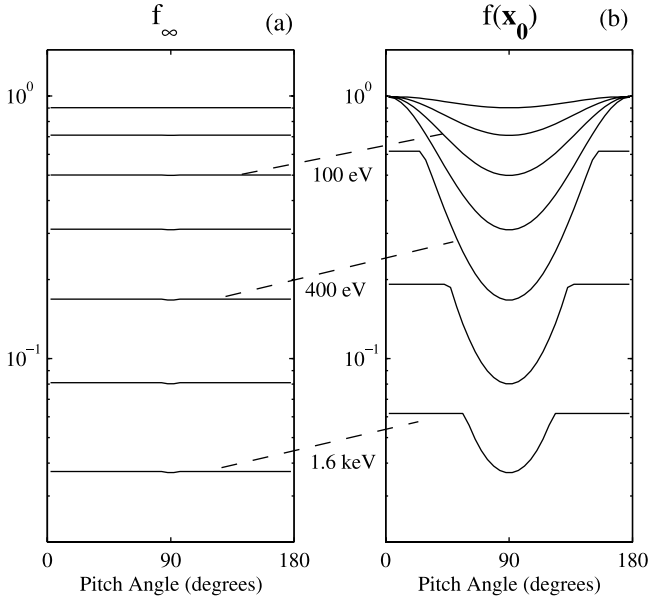

Figure 10. The distributions of Figure 9 are shown in the representation where f is given as a function of Θ for a number of different energies. The distributions are calculated for $T_e = 400$ eV and $\Phi_\parallel = 300$ V. (a) The isotropic distributions f_∞ have no dependence on Θ. (b) The trapped part of $f(\mathbf{x}_0)$ can be identified as the intervals in Θ of the well-defined dips centered on $\Theta = 90°$. For all $(\mathcal{E}, \Theta)$ we have $f_\infty(\mathcal{E}, \Theta) \le f(\mathbf{x}_0, \mathcal{E}, \Theta)$. Note that the width of the dips decreases with increasing energy.

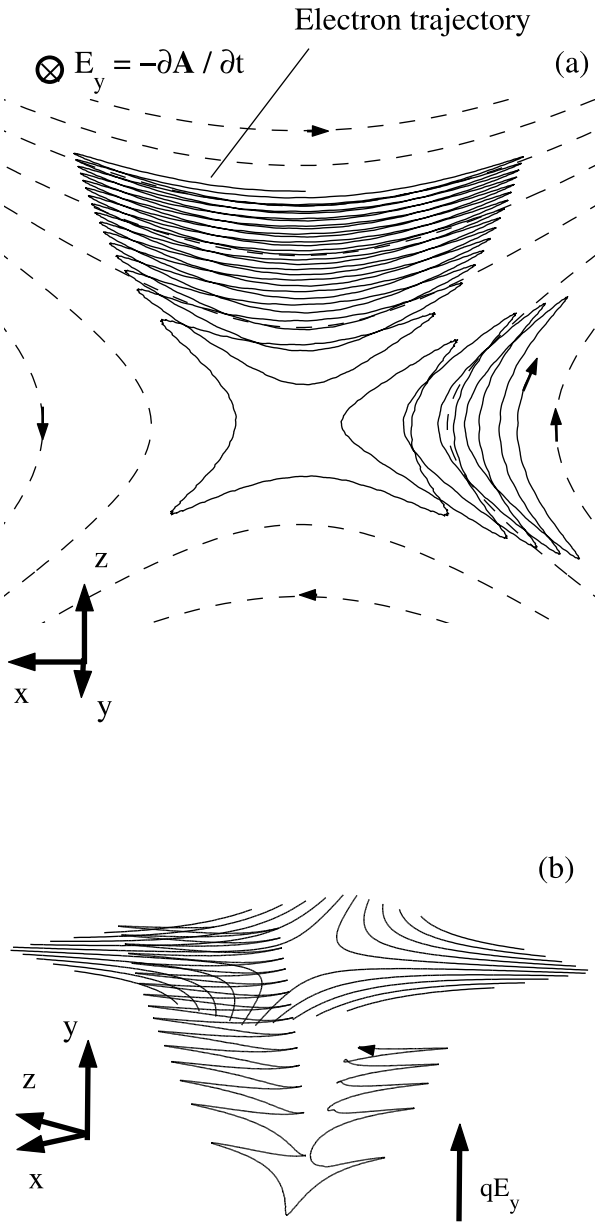

Figure 11. Example of an electron trapped magnetically in a linear cusp geometry. (a) The in-plane magnetic geometry is represented by the dashed lines. The magnetic moment of the electron is conserved due to the inclusion of a guide magnetic field B_y. The electron is ''frozen'' to one particular field line. This field line convects through the region corresponding to a finite value of the reconnection electric field, E_y. (b) Perspective view of the electron trajectory. In the inflow region, the trapped electron travels in the $-y$ direction, losing energy to the reconnection electric field.

energized by $\Phi_{\|}$. The curves are obtained for an acceleration potential $\Phi_{\|} = 300$ V and $T_e = 400$ eV. Thus the interval in Θ of trapped electrons covers all angles for $\mathcal{E}(\mathbf{x}_0) < 300$ V. The interval decreases asymptotically as $\mathcal{E}$ is increased above this value. In the limit where $\mathcal{E} \gg e\Phi_{\|}$ the electrons are passing for all Θ.

[44] As mentioned above, the derived form of f in equation (6) only depends on the local value of $\Phi_{\|}(\mathbf{x}_0)$, independent of the overall structure of $\Phi_{\|}(\mathbf{x})$ within the trapping region. The results are therefore general for any electric configuration that traps electrons. The trapping causes the phase-space density to increase $f(\mathbf{x}_0) > f_\infty$, which enhances the overall density of the electrons such that $n(\mathbf{x}_0) > n_\infty$. In contrast, for negative values of $\Phi_{\|}$ there will be no trapping and the electron density will be reduced. These observations are important, because they illustrate the role of $\Phi_{\|}$ in regulating the electron density. The condition of quasineutrality requires that the density of the electron and ions are identical; the acceleration potential will adjust such that this condition is fulfilled. Note that the acceleration potential may also influence the density of the ions.

6. Magnetic Trapping

[45] In configurations where B has a local minimum electrons can be magnetically trapped. Magnetic trapping is a consequence of the conservation of the magnetic moment $\mu = mv_\perp^2/(2B)$ and the total energy $\mathcal{E} = mv_{\|}^2/2 + \mu B$, from which it follows that $\mathcal{E}_{\|} = \mathcal{E} - \mu B$. The so-called mirror force, which is defined as $F_m = d\mathcal{E}_{\|}/dl = -\mu dB/dl$, is a force on the particle's guiding center that points along $\mathbf{B}$ in the direction of decreasing field strength. It is this force that can magnetically trap electrons (and ions) in the vicinity of a local magnetic minimum.

[46] An example of a magnetically trapped electron trajectory is given in Figure 11a. The magnetic geometry is a linear cusp, characteristic of reconnection. This configuration has a minimum in B where the in-plane magnetic field vanishes at the X-line. A guide magnetic field, B_y in the y direction is imposed such that μ is conserved everywhere. In calculating the electron trajectory a constant inductive electric field, E_y was included that corresponds to the field lines moving into and away from the X-line; it is this motion that carries the trapped electron through the region while it rapidly bounces back and forth parallel to the field.

[47] In order to study only the effects of magnetic trapping it is essential that $\mathbf{E} \cdot \mathbf{B} = 0$, so that there are no residual electric trapping effects. Because E_yB_y is finite in the considered geometry, in addition to E_y we include an in-plane electrostatic potential Φ such that $\mathbf{E} \cdot \mathbf{B} = E_yB_y - \nabla\Phi \cdot \mathbf{B}_{xz} = 0$. The detailed form of Φ is given in *Egedal and Fasoli* [2001] but here it is sufficient to know that $\mathbf{E} \cdot \mathbf{B} = 0$ such that $\Phi_{\|} = 0$ everywhere.

[48] The boundary between trapped and passing electrons depends on the conditions in the ambient plasma feeding the X-line region with electrons. We assume that the X-line configuration is embedded in a current sheet configuration where the magnetic field in the ambient plasma is B_∞. The trapped/passing boundary can then be obtained from $\mathcal{E}_{\|\infty} = \mathcal{E} - \mu B_\infty = 0$ yielding $v_{\|}/v = \cos(\Theta_b) = \sqrt{1 - B/B_\infty}$. Thus as is well known for magnetic trapping, the trapped/passing boundary, described by the pitch angle Θ_b, is independent of energy.

[49] As in the previous section, we now seek to solve equation (1) by characterizing the initial energy of the electrons in the ambient plasma. Because there are no parallel electric fields, in their single pass through the region

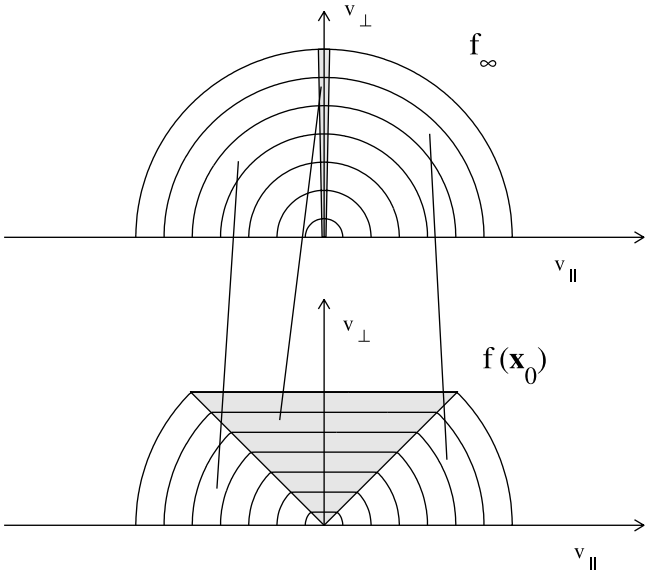

Figure 12. Illustration of the distribution function in the ambient plasma, f_∞, and in the trapping region, $f(\mathbf{x}_0)$. The magnetic trapping makes $f(\mathbf{x}_0)$ nonisotropic. Here $f(\mathbf{x}_0)$ is calculated with $B_\infty/B(\mathbf{x}_0) = 2$. Inside the trapping region (at $\mathbf{x}_0$) passing electrons have the same energy as they had in the ambient plasma. However, their pitch angles have changed from the requirement of μ being conserved. The shaded region in $f(\mathbf{x}_0)$ corresponds to trapped electrons, which all originate from a small region characterized by $|v_\parallel| \ll v_\perp$ in the ambient distributions.

the passing electrons do not experience a change in energy and it follows that

$$\mathcal{E}_\infty \simeq \mathcal{E}(\mathbf{x}_0) \qquad \text{when passing.} \tag{7}$$

[50] Meanwhile, similarly to the electrons trapped by electric fields, those that are magnetically trapped drift in the negative y direction and lose energy to E_y as they approach the X-line region. This is illustrated in Figure 11b, which is very similar to the trajectory of the electron in Figure 7 trapped in the electric fields. Again, only those electrons with $\mathcal{E}_{\parallel\infty} \simeq 0$ will be trapped. The initial energy in the ambient plasma of a magnetically trapped electron is therefore given by

$$\mathcal{E}_\infty \simeq \mu B_\infty \qquad \text{when trapped.} \tag{8}$$

Because $B_\infty > B(\mathbf{x}_0)$ it is clear that $\mathcal{E}_\perp(\mathbf{x}_0) < \mathcal{E}_\infty$, corresponding to the loss of energy against E_y as the X-line is approached.

[51] Combining equations (1), (7), and (8), the distribution $f(\mathbf{x}_0, \mathbf{v}_0)$, in the region of magnetic trapping can be expressed as

$$f(\mathbf{x}_0, \mathbf{v}_0) = \begin{cases} f_\infty(\mu B_\infty), & \text{trapped} \\ f_\infty(\mathcal{E}(\mathbf{x}_0)), & \text{passing} \end{cases}, \tag{9}$$

where the trapped/passing boundaries are now found as the solution of $\mathcal{E}_{\parallel\infty} = \mathcal{E}(\mathbf{x}_0) - \mu B_\infty = 0$ (which is equivalent to $\cos(\Theta_b) = \sqrt{1 - B/B_\infty}$). Thus in this case, because $f(\mathbf{x}_0)$ is independent of the geometry considered, it only depends on the ratio $B_\infty/B(\mathbf{x}_0)$. Equation (9) is therefore general and is valid for any configuration where electrons are magnetically trapped.

[52] Similarly to Figure 9, in Figure 12 contours of constant f_∞ and $f(\mathbf{x}_0)$ are shown in the $(v_\parallel, v_\perp)$ plane. Here $f(\mathbf{x}_0)$ is calculated for $B_\infty/B(\mathbf{x}_0) = 2$ such that the trapped/passing boundaries are $\Theta_b = 45°$ and $\Theta_b = 135°$. The energy of the passing electrons is unchanged as they enter the region so here $f(\mathbf{x}_0) = f_\infty$. Meanwhile, all the trapped electrons have their kinetic energy reduced, flattening the contours in $f(\mathbf{x}_0)$ for $45° < \Theta < 135°$.

[53] Like Figure 10, Figure 13 shows f_∞ and $f(\mathbf{x}_0)$ as functions of Θ for a number of energies. In this representation, $f(\mathbf{x}_0)$ depends on Θ only for $45° < \Theta < 135°$. Because magnetic trapping is associated with cooling we find that $f(\mathbf{x}_0, \mathbf{v}) \le f_\infty(\mathbf{v})$ for any velocity $\mathbf{v}$. It follows that magnetic trapping leads to a decrease in the plasma density inside the trapping region.

7. Quasineutrality Through Magnetic and Electric Trapping

[54] As demonstrated above, magnetic trapping leads to a decrease in the electron density. Meanwhile, inside the ion diffusion region, the ions are unmagnetized and their density is not influenced by magnetic trapping. In order for the plasma to remain quasineutral, the electron density is

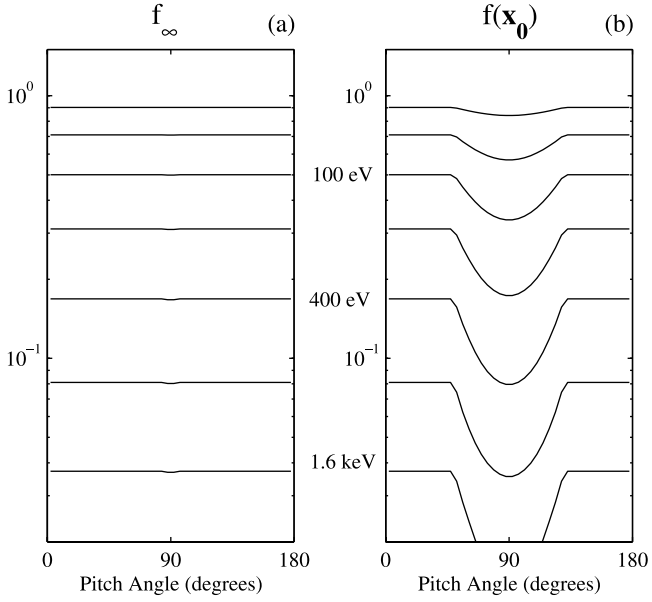

Figure 13. The distributions of Figure 12 are shown in the representation where f is given as a function of Θ for a number of different energies. (a) The isotropic distribution f_∞ has no dependence on Θ. (b) The trapped part of $f(\mathbf{x}_0)$ can be identified as the intervals in Θ of the well-defined dips centered on $\Theta = 90°$. For all $(\mathcal{E}, \Theta)$ we have $f_\infty(\mathcal{E}, \Theta) \ge f(\mathbf{x}_0, \mathcal{E}, \Theta)$. Note that the widths of the dips are independent of energy. The particular width, $45° < \theta < 135°$, is dictated by the mirror ratio $B_\infty/B(\mathbf{x}_0) = 2$.

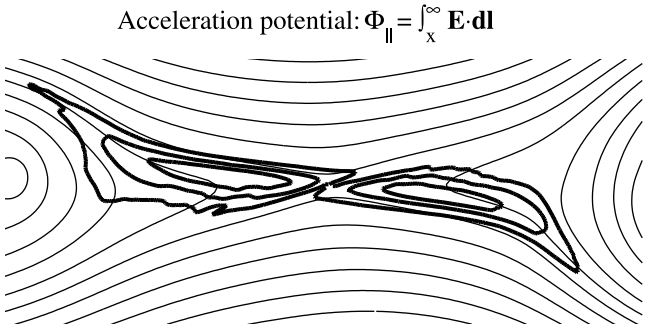

Figure 14. Example of a magnetic X-line geometry (thin lines) including an electric accleration potential, $\Phi_{\|}$ (thick lines). This $\Phi_{\|}$ is obtained from the simulation described in section 9; the asymmetry is caused by a finite guide magnetic field.

increased by electric trapping. Figure 14 provides an illustration of an *X*-line configuration including both magnetic and electric trapping.

[55] For this scenario, the mirror force does not change the energy of the passing electrons so these are still described by the "passing part" of equation (6), obtained in the case of trapping by electric fields. Furthermore, the trapped particles are also characterized by $\mathcal{E}_{\|,\infty} \sim 0$ and their magnetic moment is conserved such that their initial energy in the ambient plasma can still be expressed as μB_∞ (as it was the case for the magnetically trapped electrons analyzed above). Their distribution is therefore given by the trapped part of equation (9). Thus we find that for geometries including both electric and magnetic trapping f takes the form

$$f(\mathbf{x}_0, \mathbf{v}_0) = \begin{cases} f_\infty(\mu B_\infty) & , \text{ trapped} \\ f_\infty\big(\mathcal{E}(\mathbf{x}_0) - e\Phi_{\|}(\mathbf{x}_0)\big), & \text{passing} \end{cases}. \tag{10}$$

To characterize the trapped/passing boundaries both the electric and magnetic forces must now be taken into account as described by the solution to

$$\mathcal{E}_{\|\infty} = \mathcal{E}(\mathbf{x}_0) - e\Phi_{\|}(\mathbf{x}_0) - \mu B_\infty = 0. \tag{11}$$

[56] Figures 15 and 16 illustrate the distribution given in equation (10). Consistent with equation (11) it is seen how the trapped/passing boundaries for large $\mathcal{E}$ are dominated by the magnetic trapping, whereas for low energies they resemble those found by electric trapping in $\Phi_{\|}$. From Figure 16 it is clear that for $|v_{\|}| \ll v_\perp$ we have $f(\mathbf{x}_0) < f_\infty$ and for $|v_{\|}| \gg v_\perp$ we find the opposite, $f(\mathbf{x}_0) > f_\infty$. Thus depending on the strength of the acceleration potential and the "depth" of the magnetic well, the electron density can be either reduced or enhanced by the trapped electron dynamics.

[57] The density, n, is determined as a function of $B_\infty/B(\mathbf{x}_0)$ and $\Phi_{\|}(\mathbf{x}_0)$ by numerical integration of equation (10) over velocity space. In Figure 17, n/n_∞ is shown as a function of $\Phi(\mathbf{x}_0)$ for $B_\infty/B(\mathbf{x}_0) = 1.8$. For $\Phi_{\|}(\mathbf{x}_0) = 0$ the electron density is reduced to $n \sim 0.7\, n_\infty$. Meanwhile, for $\Phi_{\|}(\mathbf{x}_0) \simeq T_e/e$ the density is equal to that in the ambient

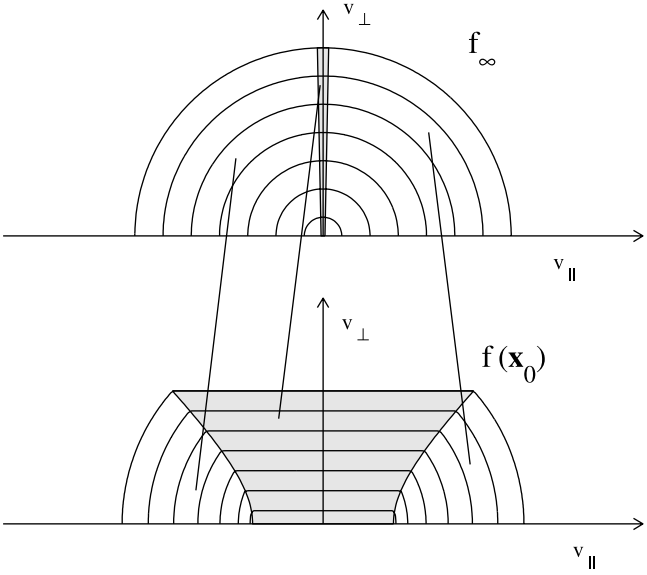

Figure 15. Illustration of how the uniform distribution f_∞ in the ambient plasma is deformed by combined electric trapping and magnetic trapping. $f(\mathbf{x}_0)$ is calculated for $B_\infty/B(\mathbf{x}_0) = 2$, $T_e = 400$ eV, and $\Phi_{\|} = 300$ V. Comparing to Figures 8 and 11 we note the similarity to the electrically trapped case for low $\mathcal{E}$ and the similarity to the magnetically trapped case for high $\mathcal{E}$.

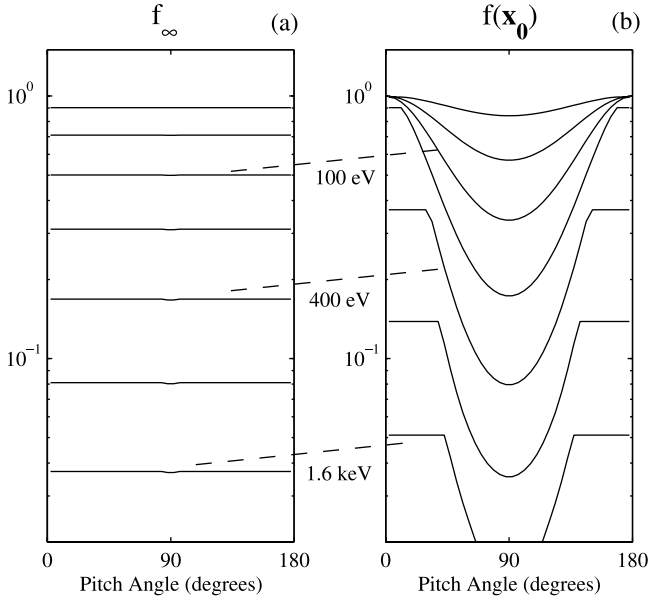

Figure 16. The distributions of Figure 15 are shown in the representation where f is given as a function of Θ for a number of different energies. (a) The isotropic distribution f_∞ has no dependence on Θ. (b) Again, the trapped part of $f(\mathbf{x}_0)$ can be identified with the intervals in Θ of the well-defined dips centered on $\Theta = 90°$. At low energies the dips cover all pitch angles, whereas at high energies the intervals of trapping approach those of magnetic trapping only, $45° < \theta < 135°$.

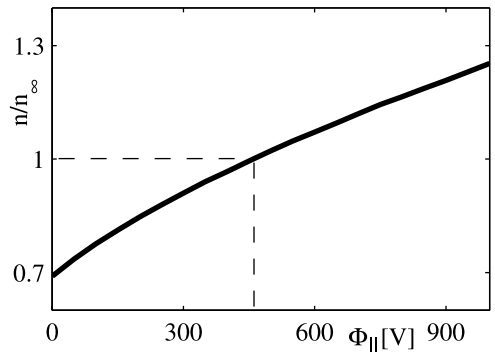

Figure 17. Electron density, n, as a function of the acceleration potential, $\Phi_{\|}$, calculated for $B_\infty/B(\mathbf{x}_0) = 1.8$ and $T_e = 400$ eV. For $\Phi_{\|} = 0$ the density is reduced due to magnetic trapping. The electron density is increased to that of the ambient plasma by including a potential, $\Phi_{\|} \simeq 450$ V ($\simeq T_e/e$).

plasma and for $\Phi_{\|}(\mathbf{x}_0) \gg T_e/e$ it can be shown that $n/n_\infty \propto \sqrt{e\Phi_{\|}(\mathbf{x}_0)/T_e}$. For a reconnection scenario where the mirror ratio is given by $B_\infty/B(\mathbf{x}_0) = 1.8$ and the ion density is constant it follows that an acceleration potential on the order of $e\Phi_{\|}(\mathbf{x}_0) \sim T_e$ is needed to boost the density to that of the ambient plasma.

8. Analysis of the Wind Data

[58] In section 3 we used numerical modeling to infer the presence of a strong acceleration potential, $\Phi_{\|} \sim 900$ V, in the reconnection event observed by the Wind spacecraft. Meanwhile, the potential can be inferred more directly (and perhaps more convincingly) from the analytic theory developed above and summarized by equation (10). From equation (10) it is clear that the passing part of $f(\mathbf{x}_0, \mathbf{v}_0)$ is isotropic. Meanwhile, the trapped part of $f(\mathbf{x}_0, \mathbf{v}_0)$ is anisotropic. This observation allows for a simple determination of $\Phi_{\|}$ from the spacecraft observations.

[59] Figures 18a and 18b show contours of the distribution function measured by Wind, which were also given above in Figure 2b. However, here we also include contours of an isotropic distribution (red dashed lines) that matches the passing part of the measured distribution. In Figure 18a the theoretically predicted trapped region corresponding to $B_\infty/B(\mathbf{x}_0) = 1.8$ and $\Phi_{\|} = 0$ is shown by the yellow area. At high energies the boundaries between passing and trapped coincide with the location where the blue contours start deviating from the red contours. However, at low energies the blue and the red contours deviate significantly outside the yellow region. We therefore conclude that magnetic trapping alone cannot account for the anisotropy in f at low energies.

[60] In Figure 18b the trapped (yellow) region is calculated with $B_\infty/B(\mathbf{x}_0) = 1.8$ and $\Phi_{\|} = 900$ V. The boundaries of the trapped region now accurately coincide with the locations where the blue and the red contours start deviating. Based on this figure alone we can conclude that $\Phi_{\|} \simeq 900$ V is the acceleration potential for the present data set.

[61] Comparing Figure 18b with $f(\mathbf{x}_0)$ in Figure 15 we notice the good agreement between the model distribution and the measured one. Nevertheless, differences are observed. For instance, the contour marked 10^{-17} in Figure 18b does not extend all the way to the trapped/passing boundary as is predicted by the theory. Below we will improve the theory to more accurately account for the observations.

[62] Out of the six assumptions listed in section 4 the second may be the most problematic. At low enough energies the magnetic moment will be conserved, but at high enough energies the electron Larmor radius will be comparable to the length scale of variation in the magnetic field. Thus the theory derived can only be expected to apply to thermal energies where μ is conserved. To extend the theory's range of validity, in this section we show that higher order corrections in the expression for μ enable equation (10) to more accurately model the Wind observations in a larger range of energies.

[63] We first apply the equations (10) and (11), including both magnetic and electric trapping, for a quantitative modeling of the Wind measurements of f displayed in Figure 2, concentrating on the near thermal energies below 2 keV. This part of the data set is also shown in Figure 19a. The corresponding theoretical distribution based on equation (10) is displayed in Figure 19b. It was calculated based on $\mu = mv_\perp^2/(2B)$ and $\Phi_{\|}(\mathbf{x}_0) = 900$ V. As in Figure 2, the curves correspond to f evaluated at the energies given to the right in the figure. For $\Theta = 0°$ (or $\Theta = 180°$) and $\mathcal{E} <$

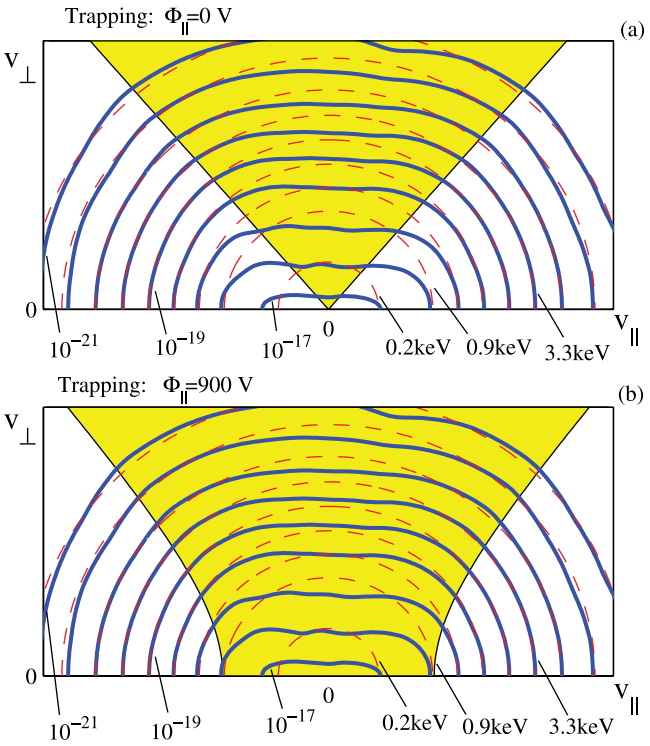

Figure 18. Contours of constant f (as measured by Wind) are given by the blue lines. For each contour f increases by a factor of $\sqrt{10}$ starting at 10^{-21} s^3 m^{-6}. The red lines represent contours of an isotropic distribution that matches the passing sections of f. (a) The area in yellow represents the region of trapping calculated with $B_\infty/B(\mathbf{x}_0) = 1.8$ and $\Phi_{\|} = 0$. (b) The trapped region is calculated for $B_\infty/B(\mathbf{x}_0) = 1.8$ and $\Phi_{\|} = 900$ V.

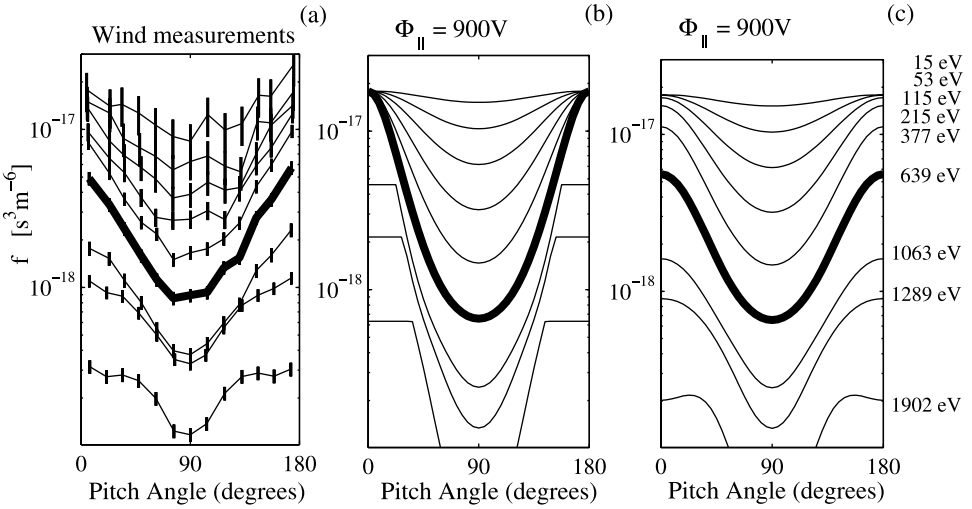

Figure 19. The curves correspond to f evaluated at the energies given to the right of the figure. (a) f measured by Wind. (b and c) Theoretical f obtained with $B_\infty/B_0 = 2$, $\Phi_{||} = 900$ V, and radius of magnetic curvature $R_B = \infty$ ($\alpha = 0$) and $R_B = 37$ km, respectively.

900 eV the theory predicts that $f = f_\infty(\mathcal{E} = 0)$, which is inconsistent with the measured distribution. The highlighted curves in Figures 19a and 19b correspond to the energy $\mathcal{E}_k$ = 639 eV; here the inconsistency between the measurements and the simple theory is clearly visible.

[64] In order for equation (10) to model the Wind measurements more accurately, μ must depend not only on $v_\perp$ but also on $v_{||}$. Such dependence has been documented for nonhomogeneous magnetic fields. In fact, $\mu = mv_\perp^2/(2B)$ is only the first term in an expansion in the small parameter m_e/e that reflects that μ is due to only the gyrating piece of $\mathbf{v}_\perp$ and drifts much be subtracted off. In *Littlejohn* [1983] these drifts are estimated and subtracted; the resulting expression for μ to the order including the relevant terms is given by

$$\mu = \frac{m}{2B}\left(W_a^2 + W_c^2\right), \quad W_a \equiv \frac{m}{e}\frac{{v_{||}}^2(bbc)}{B}, \tag{12}$$

$$W_c \equiv v_\perp - \frac{\hat{\mathbf{a}}\cdot\mathbf{E}}{B} - \frac{m}{e}\left(v_\perp v_{||}\frac{3(abc)-(cba)}{4B} + \frac{(bba)}{B}{v_{||}}^2\right).$$

In accordance with the notation of *Littlejohn* [1983] the symbols (abc), (bba), etc. are abbreviations for $(\hat{\mathbf{a}}\cdot\nabla\hat{\mathbf{b}})\cdot\hat{\mathbf{c}}$, $(\hat{\mathbf{b}}\cdot\nabla\hat{\mathbf{b}})\cdot\hat{\mathbf{a}}$, where the three unit vectors are defined by: $\hat{\mathbf{b}} \equiv \mathbf{B}/|\mathbf{B}|$, $\hat{\mathbf{c}} \equiv \mathbf{v}_\perp/v_\perp$ and $\hat{\mathbf{a}} \equiv \hat{\mathbf{b}} \times \hat{\mathbf{c}}$.

[65] The displayed Wind measurements represent the gyrophase averaged distribution. Therefore when comparing f in equation (10) to the Wind measurements we must perform the same gyrophase average over the theoretical distribution: $\langle \ldots \rangle_\phi = \oint_0^{2\pi} \ldots \, d\phi/(2\pi)$. When calculating the gyrophase average of μ in equation (12) we find that

$$\langle \mu \rangle_\phi \simeq \frac{1}{2}\frac{m}{B}\left(v_\perp^2 + \alpha {v_{||}}^4\right), \quad \alpha = \frac{m^2}{e^2B^2}\left(\hat{\mathbf{b}}\cdot\nabla\hat{\mathbf{b}}\right)^2. \tag{13}$$

It follows that $\sqrt{\alpha} = m/(eBR_B)$ where R_B is the radius of curvature of the magnetic field. Assuming that $f_\infty(\mu B_\infty)$ is linear in the range of variation in μ, we find that $\langle f_\infty(\mu B_\infty)\rangle_\phi = f_\infty(\langle\mu\rangle_\phi B_\infty)$.

[66] To illustrate the importance of the higher order corrections to μ, we consider the trajectory in Figure 20a of an electron with initial value $v_\perp = 0$ travelling out from the central region of a magnetic cusp. We notice how the electron has a helical trajectory as it leaves the figure. This

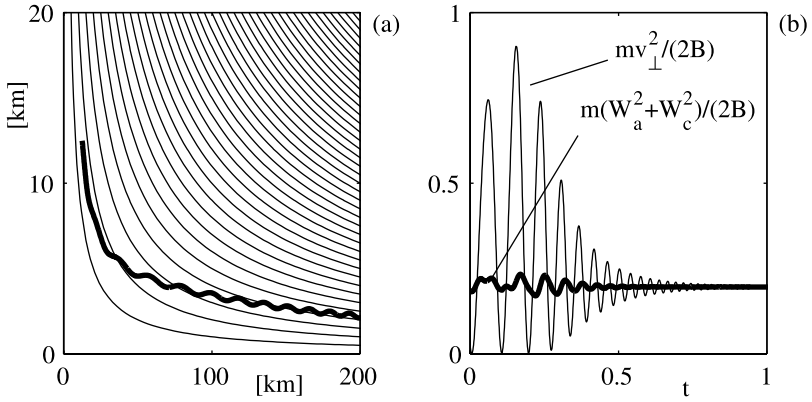

Figure 20. (a) Electron trajectory out of magnetic cusp with initial $v_\perp = 0$. (b) Two approximations for the magnetic moment as a function of time along the trajectory in a.

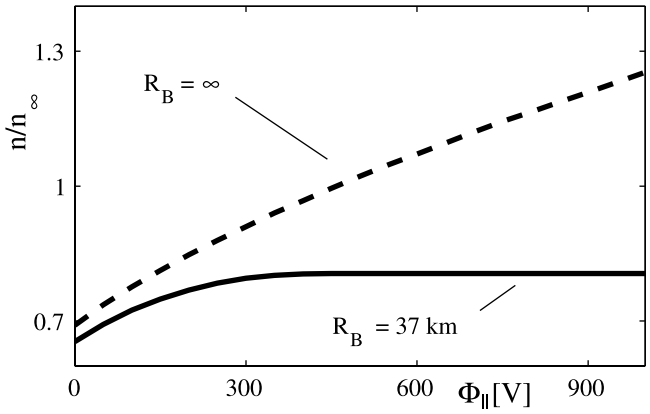

Figure 21. Electron density, n, as a function of the acceleration potential, $\Phi_{\|}$, calculated for $B_\infty/B(\mathbf{x}_0) = 1.8$ and $T_e = 400$ eV. The dashed line, obtained with $R_B = \infty$, is identical to the curve in Figure 17. The full line is obtained with $R_B = 37$ km.

is evidence that at later times it has a finite $v_\perp$ and that the "true" μ for that electron is finite.

[67] In Figure 20b the thin line represents the value of $mv_\perp^2/(2B)$ calculated along the electron trajectory. In accordance with $v_\perp = 0$ initially, for $t = 0$ we have $mv_\perp^2/(2B) = 0$. Along the trajectory large oscillations are observed in $mv_\perp^2/(2B)$ until the electron reaches the more uniform magnetic field away from the X-line. The thicker line in Figure 20b is μ evaluated along the trajectory including the higher order corrections terms as given in equation (12). This approximation for μ is always finite and agrees with the value of μ observed far away from the X-line.

[68] A measure of the overall invariance of μ is provided by the curvature parameter, $\kappa = (\sqrt{R_B/\rho_l})_{\min}$, which is the minimum value along a field line of the variable $\sqrt{R_B/\rho_l}$, where ρ_l is the Larmor radius of the considered particle. For $\kappa < 1$ the invariance of μ breaks down, leading to rapid pitch angle diffusion [*Buchner and Zelenyi*, 1989].

[69] Returning to the measured distribution displayed in Figure 2, we note that it is fully isotropic for $\mathcal{E}_k > 6$ keV. This indicates that $\kappa < 1$ at these energies. Thus it follows that $R_B \sim \rho_{l,6\mathrm{keV}}$. Evaluating the electron Larmor radius at 6 keV in a representative field of $B \sim 7$ nT we obtain the estimate $R_B \sim 37$ km. Expression (10) can now be evaluated with μ replaced by $\langle\mu\rangle_\phi$ in equation (13). The resulting f in Figure 19c provides a good match to the Wind measurements in Figure 19a, validating the theory.

[70] The deviation of μ from $\mu_0 = mv_\perp^2/(2B)$ has a fundamental influence on the dynamics of the reconnection region: the dependency of μ on $v_\|$ limits the plasma's ability to attract passing electrons from the ambient plasma, thus allowing the potential difference between the reconnection region and the outflow region to persist. This result is illustrated by the two curves in Figure 21. The curves show the electron density in the center of the reconnection region as a function of $\Phi_\|(\mathbf{x}_0)$, obtained by integrating f in equation (10) over velocity space and normalizing with respect to the density in the ambient plasma. The dashed curve represents the case where the radius of curvature in the magnetic field is infinite and the higher order terms in the magnetic moment vanish, and is identical to the curve in Figure 17. For $\Phi_\|(\mathbf{x}_0) = 0$ V, we find $n/n_\infty \sim 0.7$ corresponding to the reduction in phase space density caused by the magnetic trapping of electrons. As the potential difference $|\Phi_\|(\mathbf{x}_0)|$ is increased the density increases monotonically. For $|\Phi_\|(\mathbf{x}_0)| = 900$ V we find $n/n_\infty \sim 1.2$. Meanwhile, for the more realistic scenario represented by the solid curve in Figure 21, the radius of curvature in the magnetic field is finite and the terms in μ proportional to $v_\|^4$ are important. The dependence on $v_\|$ causes the electron density to saturate at $n/n_\infty \sim 0.8$ for potentials above 400 V.

[71] The reduced ability of $\Phi_\|$ to attract electrons from the ambient plasma (due to the $v_\|$ terms) enhances the value of $\Phi_\|$ inside the reconnection region in order to ensure quasineutrality. This may cause the electrons with energies up to several thermal energies to become trapped.

9. Electric Trapping in PIC Code Simulation of Guide Field Reconnection

[72] Trapping in electric fields has recently been documented in PIC code simulations of reconnection [*Karimabadi et al.*, 2007; *Wan et al.*, 2008]. Here we present additional and more detailed evidence for electron trapping in a simulation with parameters directly relevant to the reconnection event observed by Wind. We first consider a simulation carried out with open boundaries [*Daughton et al.*, 2006] including 2×10^9 particles in a total domain ($x \times y$) of 2048 $\times$ 2048 cells = 402.5 $\times$ 402.5 c/ω_{pe}. The simulation is translationally symmetric in the z direction and is characterized by the following parameters: $m_i/m_e = 180$, $T_i/T_e = 2$, $B_{\mathrm{guide}} = 0.5\,B_0$, $\omega_{pe}/\omega_{ce} = 2.0$, background density = 0.30 n_0 (peak Harris density), and $v_{th,e}/c = 0.20$. The time step applied was $dt = 0.065/\omega_c$. The profiles of the out-of-plane current density j_z, plasma density n_e, magnetic field B, out of plane magnetic field B_z, reconnection rate E_z, and in-plane electrostatic potential Φ, are shown in Figure 22.

[73] Of particular interest to the present analysis, in Figure 22c we notice the local reduction in the magnetic field strength B, which will cause magnetic trapping. Also, in Figure 22d the standard Hall magnetic field perturbation is observed. This perturbation has been documented extensively both theoretically and experimentally for antiparallel and near antiparallel reconnection. These Hall magnetic fields were also observed in the Wind event.

[74] Based on the electric field geometry shown in Figures 22e and 22f, it is not obvious whether the electrons are electrically trapped in the inner reconnection region. To answer this question we evaluate $\Phi_\|$ as specified in equation (2). For each point in the simulation domain the integral in equation (2) is carried out along field lines to the edge of the simulation box. The result is shown in Figure 23 where we observe a well defined region of large values of $\Phi_\|$ ranging up to 7 T_e/e (larger than the value observed by Wind). This strong acceleration potential implies that nearly all electrons carrying the main electron current channel, as displayed in Figure 22a, are trapped.

[75] Because the location of acceleration potential in Figure 23 is well defined and coincides with the central reconnection region, we conclude that the Wind spacecraft sampled the electron distribution in this inner reconnection region. To support this claim it is desirable to make a

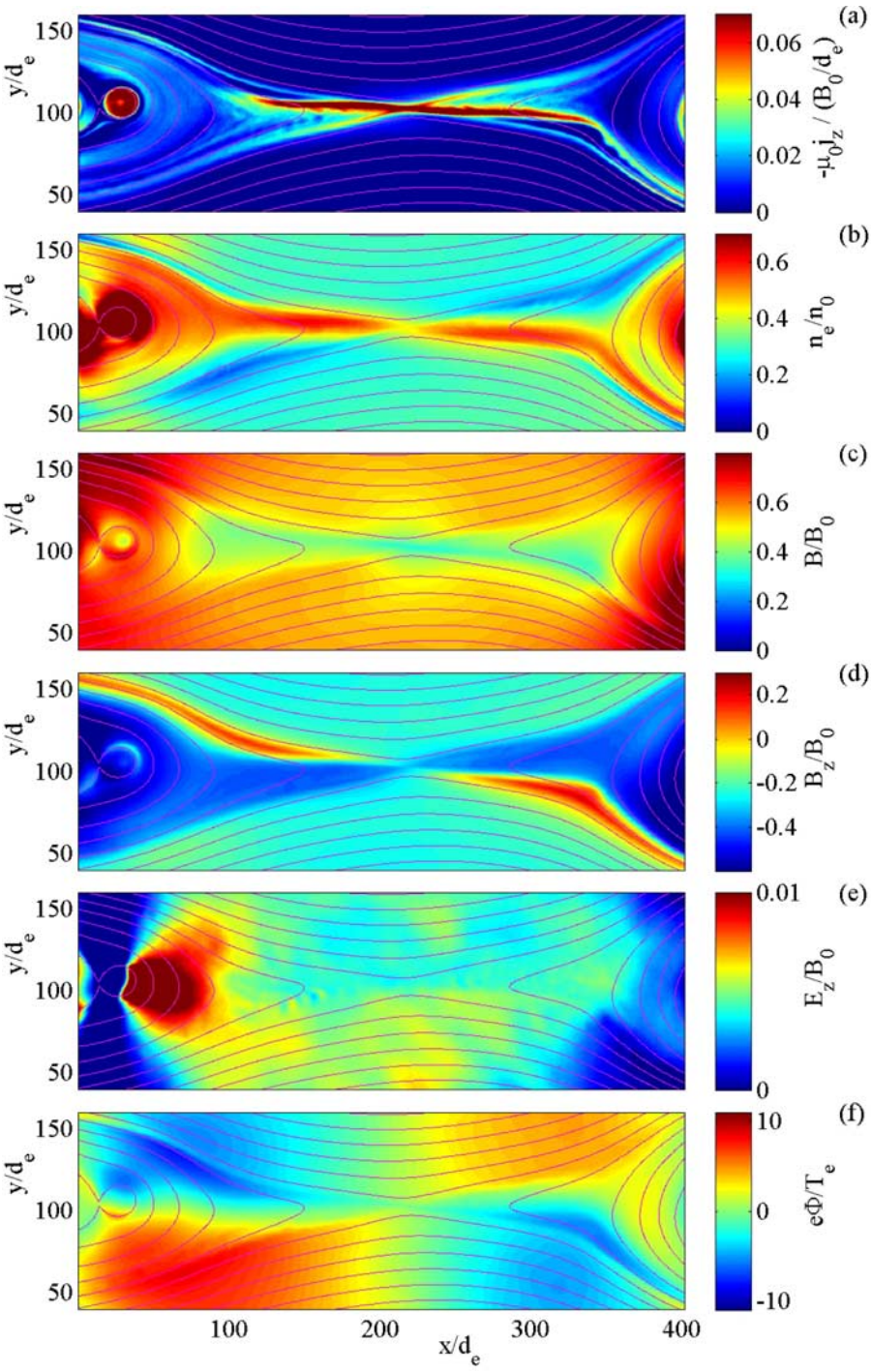

Figure 22. Color contours of j_z, n, B, B_z, E_z, and Φ, respectively. The overlayed contours of Ψ coincide with the in-plane magnetic field lines.

qualitative comparison between the distributions measured by Wind and those of the numerical simulation. While the numerical electron distributions are not readily available they can be reconstructed by applying the same methods as described in section 3. Thus we once again use Liouville's theorem $df/dt = 0$ to solve for $f(\mathbf{x}_0, \mathbf{v})$ at a point $\mathbf{x}_0$ in the inner reconnection region. From the $\mathbf{x}_0$ considered in Figure 24 we numerically follow a large number of electron trajectories back in time until they reach the point on the open boundaries where they were injected. The trajectories, an example of which is shown in Figure 24, are calculated based on the magnetic and electric fields of the time slice considered in Figure 22. The inferred distribution f is shown in Figure 25. The inferred distribution has $p_{\|}/p_{\perp} = 4.7$ which is consistent with the value of 4.8 provided directly by the simulation.

[76] At the location considered we have $\Phi_{\|}(\mathbf{x}_0) \simeq 7\ T_e/e$ causing the thermal electrons to be deeply trapped by $\Phi_{\|}$.

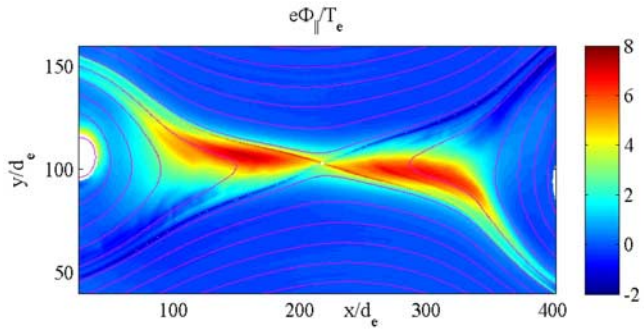

Figure 23. Contours of constant acceleration potential normalized by the temperature in the ambient plasma: $e\Phi_{\|}/T_e$.

Thus the distribution in Figure 25 has close similarities to those observed by Wind. Qualitatively, the most pronounced difference between the Wind distribution in Figure 2 and that inferred from the PIC simulation is the slight deviation from symmetry about $\Theta = 90°$ observed in Figure 25. The parallel current density is given by $j_{\|} = -e\int v_{\|} f d^3v$. Therefore if f is fully symmetric about $\Theta = 90°$, we find that $j_{\|} = 0$. In turn, the deviation from symmetry, controlled by the orbit dynamics, causes a finite overall flow of the electrons along field lines needed in order to account for the current channel in Figure 22a.

[77] It should be noted that the PIC calculation is carried out with $m_i/m_e = 180$ reducing the thermal speed of the electrons. Thus at the natural mass ratio a given parallel current density can be caused by smaller asymmetries in f. Therefore although the f measured by Wind is more symmetric than that inferred from the simulation, the level of asymmetry may be consistent in terms of the total current density carried by the trapped electrons.

[78] The open boundary conditions of the simulation effectively allow the simulation to be compatible with the dynamics of a much larger system. Although the simulated reconnection geometry is asymmetric about the X-line, it can be shown that the simulation is compatible with the assumption applied here (see Figure 5) that the X-line region is embedded in a uniform current sheet. This will be documented in future publications now in preparation. By taking moments of the analytical distribution function

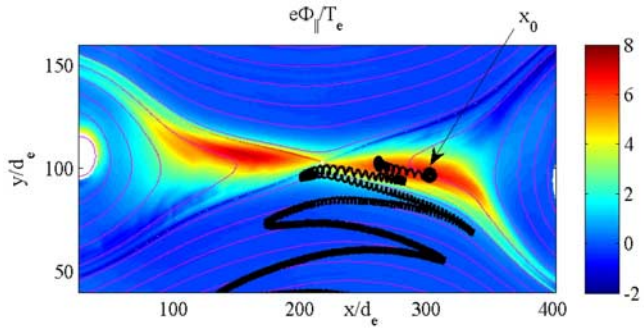

Figure 24. Example of a trapped electron overlayed on color contours of constant $\Phi_{\|}$. The end point $\mathbf{x}_0$ of this orbit is the location at which the distribution in Figure 25 is evaluated.

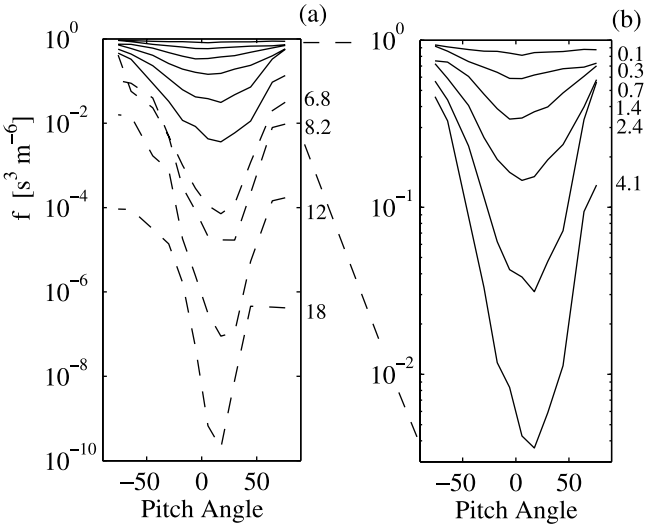

Figure 25. Inferred electron distribution computed based on the electric and magnetic field geometry of a PIC simulation. Each curve shows f as a function of pitch angle for a particular energy given to the right of each curve (normalized to the electron temperature in the ambient plasma). (a) Electrons with energies above $e\Phi_{\|}$, are represented by the dashed lines. Here the values of f are small and they do not significantly influence the overall reconnection dynamics. (b) The solid lines of a are repeated to zoom-in on the thermal part of the distribution.

derived above a new kinetic fluid model is obtained. We find that this fluid model, among other results, accurately reproduces profiles of $\Phi_{\|}$, $p_{\|}$ and $p_{\perp}$ from the present simulation.

[79] The acceleration potential and the described physics of the trapped electrons do not appear to be dependent on the choice of boundary conditions. This is evident from Figure 26, which illustrates that the $\Phi_{\|}$ of a P3D code simulation with periodic boundaries [*Zeiler et al.*, 2002] is nearly identical to $\Phi_{\|}$ of the open boundary simulation in Figure 23.

10. Role of Trapping in Fast Reconnection

[80] For both the Wind event and the PIC simulation we have shown that the thermal electrons are trapped electri-

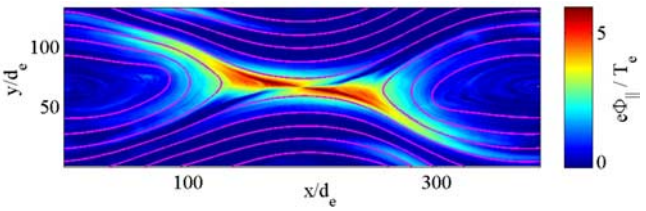

Figure 26. Acceleration potential $\Phi_{\|}$ from a simulation with periodic boundary conditions [*Zeiler et al.*, 2002]. This simulation is characterized by $T_i/T_e = 1$, $B_{\text{guide}} = 0.5\ B_0$, $m_i/m_e = 225$, background density $= 0.5\ n_0$, and about $2 \cdot 10^8$ particles in a domain of 2048×1024 cells $= 392 \times 196\ c/\omega_{pe}$.

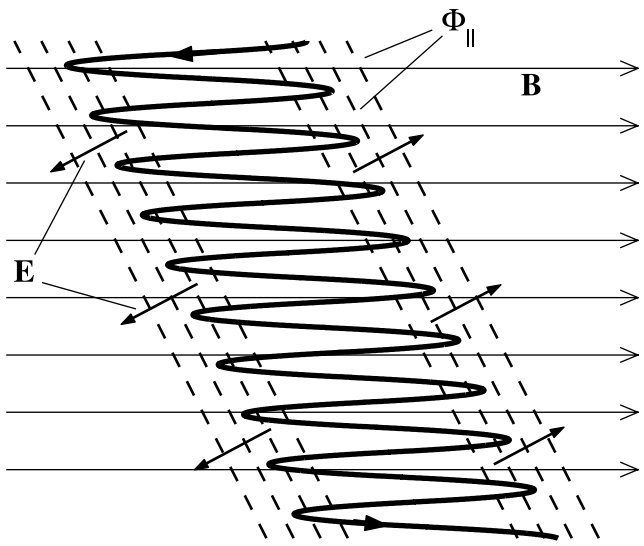

Figure 27. Illustration of a trapped electron with a net drift velocity along the magnetic field. The parallel drift is controlled by the acceleration potential $\Phi_{||}$ oblique to the uniform magnetic field.

cally. The trapping imposes strict constraints on the form of the electron distribution that are important to the overall reconnection dynamics. In fact, the expression derived for f in equation (10) is fully symmetric in Θ about $\Theta = 90°$. Therefore according to this theory the trapped electrons can carry no parallel currents: $j_{||} = \int v_{||} f d^3v = 0$. This result, however, is not consistent with the PIC simulation where we clearly observe that $j_{||} \neq 0$. As is mentioned in section 4, the inconsistency is linked to an assumption we made in deriving equation (10); namely that the thermal speed of the electrons is much larger than any other velocity in the system. In the limit of small electron mass (high electron thermal speed) equation (10) provides a valid approximation for f, but because the electron mass is finite (and thus $v_{th} < \infty$) it does not capture the asymmetries about $\Theta = 90°$ associated with parallel currents.

[81] To understand how trapped electrons can carry a parallel current it is useful to consider the configuration in Figure 27. Here an electron is confined by a acceleration potential that is oblique to the uniform magnetic field. As the electron moves downward with the magnetic field lines the acceleration potential causes the electron to move to the right along the uniform magnetic field. While the geometry of the reconnection region is significantly more complicated, this simple cartoon describes the basic physical mechanism controlling the parallel current in the reconnection region. Therefore the parallel currents of trapped electrons are fully governed by the geometric structure of the acceleration potential.

[82] One caveat is that the acceleration potential in Figure 23 (and also in Figure 26) is small on the two of the four separators. The low values of $\Phi_{||}$ coincide with the areas of density depletion (see Figure 22b), which is a well known signature in guidefield reconnection [*Pritchett and Coroniti*, 2004; *Cattell et al.*, 2005]. Thus in the areas of density depletion the plasma current is not regulated by trapping and the free streaming of electrons is not prohibited. It should also be noted that electron currents in the reconnection region can be carried by the various drifts of electrons perpendicular to the magnetic field lines (including E × B drifts, curvature drifts, and grad B drifts).

[83] Nevertheless, based on the analysis above it is clear that in significant areas of the reconnection region large values of $\Phi_{||}$ are observed. In these areas, the resultant trapping is effective in limiting the parallel currents because the free streaming along field lines is eliminated. Applying the language of magnetic fusion research, the trapping implies a large neoclassical impedance. This allows reconnection to proceed at a high rate. The physics of the trapped electrons can be expected to be particularly important for guide field reconnection, because here the X-line is aligned with the magnetic field. Without trapping free steaming electrons could dramatically influence the in-plane magnetic geometry and slow reconnection.

[84] Within the two-fluid formulation the orbit kinetic effects are included in the pressure tensor, **p**. Therefore the full pressure tensor, **p**, must be obtained in order for the (collisionless) generalized Ohms's law,

$$\mathbf{E} + \mathbf{v} \times \mathbf{B} = \frac{1}{ne}(\mathbf{j} \times \mathbf{B} - \nabla \cdot \mathbf{p}) + \frac{m}{ne^2}\frac{d\mathbf{j}}{dt},$$

to correctly include the effects of trapping on the electric fields in the reconnection region. The theoretical distribution derived above is rotationally symmetric about the

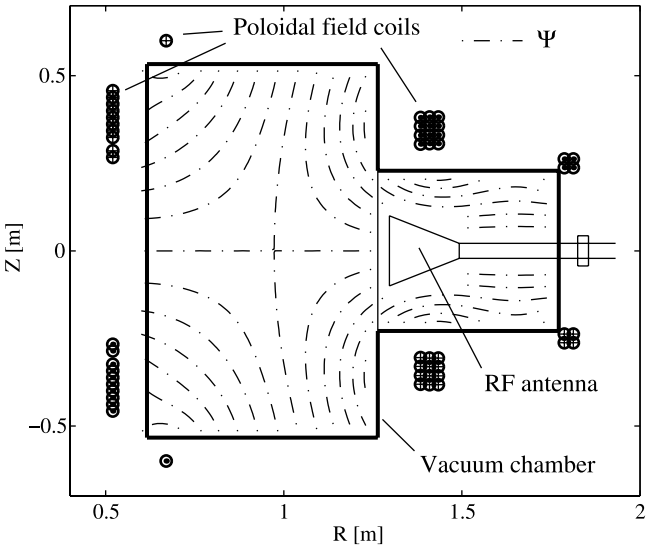

Figure 28. Poloidal cross-section of VTF open configuration. The dashed contour lines correspond to constant levels of the poloidal magnetic flux, Ψ, which coincide with magnetic field lines. Due to the boundary conditions, all electrons in this configuration are trapped.

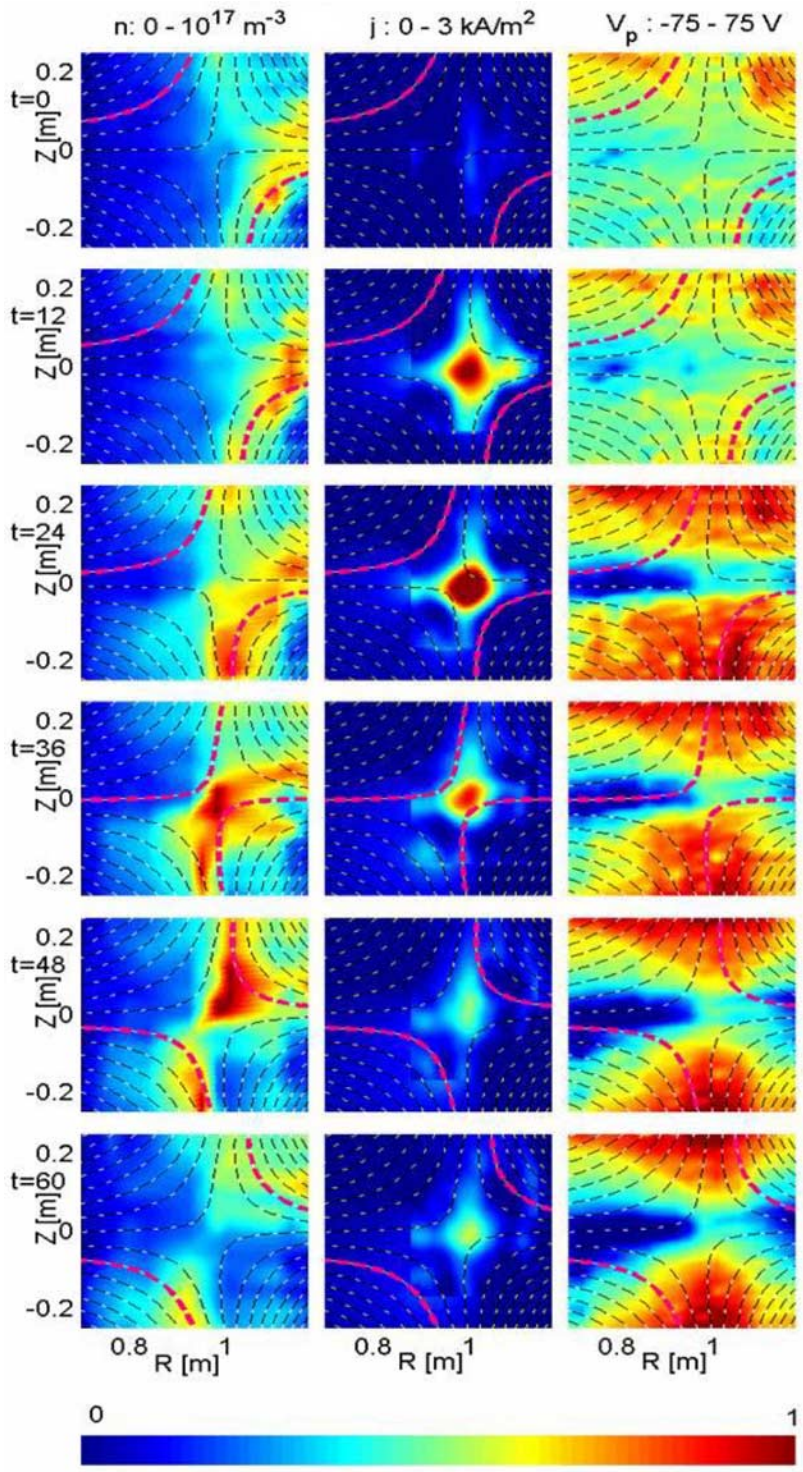

Figure 29. Measured contours of number density, plasma current, and electrostatic potential during the initial phase of driven reconnection in VTF. Each row of subfigures corresponds to a snapshot in time as indicated on the left-hand side. Between each row, the time is incremented by 12 μs.

magnetic field direction, but includes different parallel and perpendicular pressures, such that $\mathbf{p} = p_{\|}\hat{\mathbf{b}}\hat{\mathbf{b}} + (\mathbf{I} - \hat{\mathbf{b}}\hat{\mathbf{b}})p_{\perp}$. Thus in our model the parallel electric fields are balanced by the well known terms of a diagonal pressure tensor: $-enE_{\|} = \hat{\mathbf{b}} \cdot (\nabla \cdot \mathbf{p}) = \nabla_{\|}p_{\|} + (\nabla_{\|}B)(p_{\|} - p_{\perp})/B$. Therefore the reduction in parallel currents caused by trapping is not associated with gyroviscosity (off-diagonal pressure), which is important for balancing the reconnec-

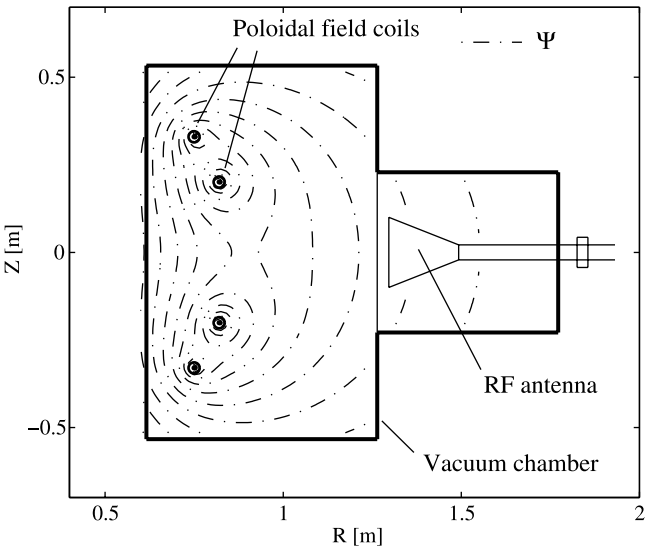

Figure 30. Poloidal cross-section of VTF closed configuration. The magnetic geometry, represented by the dashed lines, is generated by four in-vessel coils. The geometry is compatible with toroidally passing electrons.

tion electric field within a few ρ_e of the X-line [*Hesse*, 2006].

11. Laboratory Investigations of Electron Trapping in Reconnection

[85] Electron trapping has been found to be important to reconnection also in laboratory plasmas. In fact, the analysis of the Wind event summarized in section 3 was directly inspired by experimental results in the Versatile Toroidal Facility (VTF) located at the Plasma Science and Fusion Center at the Massachusetts Institute of Technology [*Egedal et al.*, 2000].

[86] The VTF device facilitates experiments with two distinct sets of boundary conditions: an ''open'' configuration in which the field lines intersect the vacuum vessel walls, and a ''closed'' configuration in which the magnetic field lines form closed loops inside the device. Typically, the experiment is operated with a guide magnetic field about 30 times stronger than the in-plane magnetic field.

[87] For the open configuration illustrated in Figure 28 electron trapping is so efficient in limiting the plasma current that in the driven scenario reconnection proceeds at the rate imposed externally. The trapped electron dynamic is closely linked to the boundary conditions where all magnetic field lines (except for the X-line) intersect the vacuum vessel walls. Because electrons are tied to magnetic field lines they become trapped continuously moving back and forth along field lines, bouncing in the electrostatic sheaths at the boundary layer between the plasma and the walls.

[88] The data in Figure 29 represents the measured time evolution of the density, current and potential profiles for a Hydrogen plasma. The data is acquired in the initial phase after the inductive reconnection drive is switched on at $t = 0$. The profiles of the number density, current density and electrostatic potential are obtained by movable electrostatic and magnetic probe arrays. Data is collected during a large number of discharges, taking advantage of the high degree of shot-to-shot reproducibility. The profiles of the three components of **B** are obtained from magnetic probe measurements. The plasma currents are calculated through $\mu_0\mathbf{j} = \nabla \times \mathbf{B}$, assuming toroidal symmetry. The dashed lines in all the subfigures represent magnetic field lines, inferred on the basis of the toroidal plasma current profile and the currents applied in the VTF coil sets. Two magnetic field lines, corresponding to one particular value of the poloidal magnetic flux function Ψ, are highlighted in pink so that they can be followed in time as they drift together, reconnect, and drift apart.

[89] The importance of trapping is illustrated by the low current density observed. The total toroidal current is on the order of 20 A, whereas a simple calculation applying classical Spitzer resistivity yields an expected value of about 20 kA. Although the plasma parameters and magnetic geometry are quite different from those of the Wind reconnection event, an analysis using Liouville's theorem also successfully accounted for the small parallel current observed in the experiment [*Egedal et al.*, 2004].

[90] Further experimental evidence for the effectiveness of trapping in eliminating parallel currents is provided when the results of the open VTF configuration are compared to those of the closed configuration in VTF. As shown in Figure 30 in the closed configuration the field lines are contained inside the device allowing the electrons to be toroidally passing. Thus in this closed configuration the total plasma current is increased by a factor of 10^3 compared to the open configuration [*Egedal et al.*, 2005].

12. Conclusion

[91] An analytical model for the major features of anisotropy in the electron distribution function has been developed. This model applies to reconnection geometries including a guide magnetic field such that the magnetic moments of the electrons are conserved. The model successfully accounts for the anisotropic features observed in situ by the Wind spacecraft in a reconnection region in the deep magnetotail. Furthermore, the model shows that magnetic trapping decreases the electron density and that additional electrical trapping is necessary to increase the electron density and maintain quasineutrality in the reconnection region. The presence of electric trapping is also demonstrated for a PIC code simulation of guide field reconnection.

[92] Electric trapping is important because it eliminates the free streaming of electrons along field lines, thereby significantly altering the conductive properties of the plasma inside the reconnection region. Thus we conclude that trapping helps speed the rate of collisionless reconnection.

[93] **Acknowledgments.** Fruitful discussions and collaboration with Prof. G. Lapenta are gratefully acknowledged. This work was partly funded by NASA grant NNG05GH18G at Berkeley and DOE Junior Faculty award ER54878 and NSF/DOE award PHY-0613734 at MIT.

[94] Amitava Bhattacharjee thanks the reviewers for their assistance in evaluating this paper.

References

Buchner, J., and L. M. Zelenyi (1989), Regular and chaotic charge-particle motion in magnetotail-like field reversals: 1. Basic theory of trapped motion, *J. Geophys. Res.*, *94*, 11,821–11,842.

Cattell, C., et al. (2005), Cluster observations of electron holes in association with magnetotail reconnection and comparison to simulations, *J. Geophys. Res.*, *110*, A01211, doi:10.1029/2004JA010519.

Daughton, W., G. Lapenta, and P. Ricci (2004), Nonlinear evolution of the lower-hybrid drift instability in a current sheet, *Phys. Rev. Lett.*, *93*, 105004.

Daughton, W., J. Scudder, and H. Karimabadi (2006), Fully kinetic simulations of undriven magnetic reconnection with open boundary conditions, *Phys. Plasmas*, *13*, 072101.

Drake, J. F., M. Swisdak, and C. Cattell (2003), Formation of electron holes and particle energization during magnetic reconnection, *Science*, *299*, 873.

Egedal, J., and A. Fasoli (2001), Single-particle dynamics in collisionless magnetic reconnection, *Phys. Rev. Lett.*, *86*, 5047.

Egedal, J., A. Fasoli, M. Porkolab, and D. Tarkowski (2000), Plasma generation and confinement in a toroidal magnetic cusp, *Rev. Sci. Instrum.*, *71*, 3351.

Egedal, J., W. Fox, E. Bolonohy, and M. Porkolab (2004), Kinetic simulation of the VTF magnetic reconnection experiment, *Comput. Phys. Commun.*, *164*, 29.

Egedal, J., M. Øieroset, W. Fox, and R. P. Lin (2005), In situ discovery of an electrostatic potential, trapping electrons and mediating fast reconnection in the earth's magnetotail, *Phys. Rev. Lett.*, *94*, 025006.

Giovanelli, R. G. (1946), A theory of chromospheric flares, *Nature*, *158*, 81.

Hesse, M. (2006), Dissipation in magnetic reconnection with a guide magnetic field, *Phys. Plasma*, *13*, 122107.

Karimabadi, H., W. Daughton, and J. Scudder (2007), Multi-scale structure of the electron diffusion region, *Geophys. Res. Lett.*, *34*, L13104, doi:10.1029/2007GL030306.

Lin, R. P., et al. (1995), A 3-dimensional plasma and energetic particle investigation for the Wind spacecraft, *Space Sci. Rev.*, *71*, 125.

Littlejohn, R. G. (1983), Variational-principles of guiding center motion, *J. Plasma Phys.*, *29*, 111–125.

Nagai, T., I. Shinohara, M. Fujimoto, M. Hoshino, Y. Saito, S. Machida, and T. Mukai (2001), Geotail observations of the Hall current system: Evidence of magnetic reconnection in the magnetotail, *J. Geophys. Res.*, *106*, 25,929.

Øieroset, M., T. D. Phan, M. Fujimoto, R. P. Lin, and R. P. Lepping (2001), In situ detection of collisionless reconnection in the Earth's magnetotail, *Nature*, *412*, 414.

Øieroset, M., R. P. Lin, T. D. Phan, D. E. Larson, and S. D. Bale (2002), Evidence for electron acceleration up to similar to 300 keV in the magnetic reconnection diffusion region of Earth's magnetotail, *Phys. Rev. Lett.*, *89*, 195001.

Phan, T. D., J. F. Drake, M. A. Shay, F. S. Mozer, and J. P. Eastwood (2007), Evidence for an elongated (>60 ion skin depths) electron diffusion region during fast magnetic reconnection, *Phys. Rev. Lett.*, *99*, 255002.

Priest, E., and T. Forbes (2000), *Magnetic Reconnection*, Cambridge Univ. Press, Cambridge, U.K.

Pritchett, P. L., and F. V. Coroniti (2004), Three-dimensional collisionless magnetic reconnection in the presence of a guide field, *J. Geophys. Res.*, *109*, A01220, doi:10.1029/2003JA009999.

Sonnerup, B. U. O., G. Paschmann, and T. D. Phan (1995), *Fluid Aspects of Reconnection at the Magnetopause: In Situ Observations, Physics of the Magnetopause*, *Geophys. Monogr. Ser.*, vol. 90, p. 167, AGU, Washington, D. C.

Vasyliunas, V. M. (1975), Theoretical models of magnetic-field line merging, *Rev. Geophys. Space Phys.*, *13*, 303.

Wan, W., G. Lapenta, G. L. Delzanno, and J. Egedal (2008), Electron acceleration during magnetic reconnection, *Phys. Plasma*, *15*, 032903.

Wygant, J. R., et al. (2005), Cluster observations of an intense normal component of the electric field at a thin current sheet in the tail and its role in the shock-like acceleration of the ion fluid into the separatrix region, *J. Geophys. Res.*, *110*, A09206, doi:10.1029/2004JA010708.

Zeiler, A., D. Biskamp, J. F. Drake, B. N. Rogers, and M. A. Shay (2002), Three-dimensional particle simulations of collisionless magnetic reconnection, *J. Geophys. Res.*, *107*(A9), 1230, doi:10.1029/2001JA000287.

W. Daughton, Plasma Theory and Applications, Los Alamos National Laboratory, X-1-PTA, Los Alamos, NM 87545, USA.

J. F. Drake, Laboratory for Plasma Research, University of Maryland, Williams Building, College Park, MD 20742, USA.

J. Egedal, Plasma Science and Fusion Center and Physics Department, Massachusetts Institute of Technology, 16 Albany Street, NW16-132, Cambridge, MA 02139, USA. (jegedal@psfc.mit.edu)

W. Fox, Plasma Science and Fusion Center, Massachusetts Institute of Technology, Albany Street 167, NW16-135, Cambridge, MA 02139, USA.

N. Katz, Plasma Science and Fusion Center, Massachusetts Institute of Technology, Albany Street 167, NW16-133, Cambridge, MA 02139, USA.

R. P. Lin and M. Øieroset, Space Sciences Laboratory, University of California, 7 Gauss Way, Berkeley, CA 94720-7450, USA.

M. Porkolab, Plasma Science and Fusion Center, Massachusetts Institute of Technology, Albany Street 167, NW16-288, Cambridge, MA 02139, USA.